A method for characterizing the spatial organization of deep convective cores in deep convective systems' cloud shield using idealized elementary convective structure decomposition

Louis Netz[1], Thomas Fiolleau[1] and Rémy Roca[1]

[1] Université de Toulouse, Laboratoire d'Etudes en Géophysique et Océanographie Spatiales (CNRS/CNES/IRD/UPS), Toulouse, France

Corresponding author: Louis Netz (louis.netz@cnrs.fr)

ORCID: Louis Netz 0009-0009-2112-8453

ORCID: Thomas Fiolleau 0000-0001-5902-1701

ORCID: Rémy Roca 0000-0003-1843-0204

Abstract

Deep convective systems (DCSs) play a fundamental role in atmospheric dynamics, precipitation, cloud radiative effects, and large-scale circulations. Their associated deep convection exhibits complex spatial arrangements, commonly referred to as convective organization, which exerts an influence on the systems' morphology that needs to be assessed. However, quantifying this organization remains challenging due to the lack of a general, robust, and consensual metric, in both observations and models. This study introduces a new method for characterizing the spatial arrangement of deep convective cores within the cloud shield of individual DCSs. The first step of this technique consists in decomposing the convective mask into elementary structures. Four key ~~variables~~parameters are then extracted to fully capture the organization of a scene. Two of these ~~variables~~parameters characterize the overall properties of the convective field, such as the size and convective fraction of convective cores. The remaining two ~~variables~~parameters are specifically designed to describe the spatial arrangement of deep convective cores: a characteristic convective scale using two-dimensional (2D) autocorrelation and an evaluation of the deviation from randomness by comparing it to a stochastic ensemble of synthetic convective fields. Two independent datasets, derived from satellite observations and idealized kilometer-scale numerical simulations, each employing distinct convective core identification techniques are used to assess the generalization of the method. Finally, an unsupervised clustering algorithm identifies four distinct classes, revealing consistent and physically sound patterns of convective organization across both datasets. This demonstrates the method's robustness and suitability to characterize the spatial organization of convective cores in convective systems' cloud shield.

Short summary:

Large convective systems are the primary drivers of the Earth's rainfall and climate, yet the spatial organization of their associated convection remains poorly described. This study presents a straightforward approach to characterizing this organization. First, the convective field is decomposed into elementary structures, and then four scores are computed to describe cores' size, density, spacing

39 scale, and departure from randomness. Applied to both satellite data and km-scale simulations, the
40 method robustly yields the same overall organization characterization.

1 Introduction

42 In the atmosphere, deep convection occurs mainly in the form of structures where multiple individual
43 convective cells are spatially organized yielding to a wide diversity of convective cloud systems, ranging
44 from hurricanes to squall lines (Lafore et al. 2017). The largest and longest lived of these systems are often
45 termed Mesoscale Convective System and are also characterized by a specific organization of deep
46 convection inside the cloud system's shield (Houze 2004). Yet, the reasons for this organization remain
47 challenging to assess (Muller et al. 2022). Large scale forcing is often invoked (Markowski and Richardson
48 2010) and cell to cell interaction (Mapes 1993) is also a process identified to explain the self-organization
49 of deep convection in the absence of large scale forcing as observed in the tropics (LeMone, Zipser, and
50 Trier 1998; Holloway et al. 2017). Recent investigation suggests radiative feedback between the cloud
51 and convection also contribute to the organization of deep convection (Muller and Bony 2015; Wing and
52 Emanuel 2014). The consolidation of our physical understanding of the role of deep convection
53 organization is nevertheless hampered by the lack of ~~an~~a univocal definition of organization (Retsch,
54 Jakob, and Singh 2020).

55 Indeed, if anything organization is a loose term. Encompassing descriptive perspective (Gallus, Snook, and
56 Johnson 2008) to mathematical formulation (e.g., Tobin, Bony, and Roca 2012), organization refers to
57 various spatial arrangements. Departure of such arrangement from randomly arranged low level cloud
58 fields has been a starting point of numerous investigations that prompted complementary concepts like
59 clustering and regularity (Weger et al. 1992). Recently, these concepts were integrated into a single metric
60 that could discern regular, random, and clustered cloud scenes (Biagioli and Tompkins 2023; Tompkins
61 and Semie 2017). The relevance of such indices to the specificity of deep convection within a convective
62 cloud shield is not straightforward. First, owing to its formulation, a minimum number of convective cores
63 is required to compute the metrics (Mandorli and Stubenrauch 2023); a criterion which is not easily
64 ~~met~~satisfied for deep convective systems (Schiro et al. 2020). Second, most of the metrics are computed
65 over a given regular area in contrast with the variable nature of the deep convective systems cloud shield
66 area (Roca, Fiolleau, and Bouniol 2017). Finally, another source of difficulty arises from the very definition
67 of deep convection, be it point wise or object oriented (Takahashi et al. 2023). Other existing metrics that
68 are more object oriented such as COP, ABCOP and ROME (White et al. (2018), Jin et al. (2022), Retsch et
69 al. (2020)) consider different convection parameters, like the object's area, mean area of objects, relative
70 or geometric distance between objects, in addition to their center within a specific grid.

71 Building on previous efforts and acknowledging their respective strengths and limitations, we introduce a
72 novel approach that employs an algorithm to compute organizational metrics of deep convective cores.
73 These computations are conducted across multiple scenes characterized by varying extents of DCSs' cloud
74 shield. This ensemble of scenes is then classified to reveal four, well separated, unambiguous classes of
75 organization. The procedure is performed on two datasets using different identification of deep
76 convection, a hydrometeor and a dynamical perspective, to assess the sensitivity of the overall method
77 to the definition of deep convection. The article is articulated as follows. Section 2 introduces the data
78 and the convective core identification. Section 3 summarizes the algorithm and its implementation. A
79 summary and discussion are offered in section 4 and a conclusion section ends the paper.

2 Data

2.1 Satellite observations

Georing Infrared Observations

Thermal infrared brightness temperature data from the operational meteorological geostationary satellite fleet (GEOring) were used to monitor deep convective systems across the tropical belt throughout the 2012–2020 period. As highlighted by Fiolleau et al. (2020), the GEOring is not a homogeneous suite of instruments operating under uniform conditions. Differences in spatial and temporal resolution, spectral filter functions, and calibration procedures vary between platforms, leading to systematic biases in brightness temperature measurements. To address these discrepancies, Fiolleau et al. (2020) homogenized thermal infrared data from the geostationary satellite fleet for cold cloud studies, using the Scanner for Radiation Budget (ScaRaB) IR channel onboard Megha-Tropiques as a reference. The resulting GEOring IR dataset was inter-calibrated, spectrally adjusted, and corrected for limb darkening over a nine-year period.

To complete the harmonization process, the temporal resolution was standardized to 30 minutes across the GEOring, and all geostationary data were remapped onto a common 0.04° equal-angle longitude-latitude grid (Fiolleau et al., 2020). The spatial coverage of each geostationary platform was selected to provide substantial overlap with adjacent satellites, ensuring seamless data continuity between 55°S and 55°N. The fully homogenized IR GEOring dataset is comprehensively described in Fiolleau et al. (2020) and Fiolleau & Roca (2024).

Convective System cold cloud shield from the TOOCAN algorithm

The TOOCAN algorithm is a 3D segmentation-based method designed to track Deep Convective Systems (DCSs) using geostationary infrared (IR) satellite imagery. It identifies DCSs within a time series of IR images through a spatio-temporal region-growing technique, which iteratively detects and expands convective seeds. If present, convective seeds are first identified at 190 K, requiring a minimum lifetime of 1h30 (3 frames) and an area of at least 625 km² per frame. These are then dilated using a 10-connected spatiotemporal neighborhood operator until reaching a boundary that is 2 K warmer. A second convective seed detection is subsequently applied at 192 K. This iterative process continues, progressively expanding the identified seeds and detecting new ones at every 2 K increment, until reaching the 235 K boundary (Fiolleau and Roca, 2013).

The algorithm decomposes the high cold cloud shield below 235 K into multiple DCSs, even when their anvil clouds are interconnected. This approach enables a comprehensive identification of DCSs, ranging from small, short-lived, isolated systems to long-lived, extensive convective systems that can propagate over several hundred kilometers and span several thousand square kilometers. More importantly, TOOCAN suppresses split and merge artefacts, a key limitation of traditional overlap-based tracking methods. By capturing the full spectrum of convective system organization, TOOCAN improves the representation of convective evolution, offering a more reliable characterization of deep convective systems (DCSs).

In this study, we use a database of deep convective systems and their morphological characteristics covering the 2012–2020 period over the intertropical belt, fully described in Fiolleau and Roca (2024). TOOCAN has been systematically applied to the homogenized GEOring IR data over this period. The resulting database provides access to key morphological parameters of each DCS, including its location and time of initiation and dissipation, lifetime duration, propagation distance, and maximum cold cloud

122 extent. Additionally, the dataset documents the evolution of morphological properties throughout the
123 DCS life cycle. A total of 15×10^6 DCSs have been detected and tracked by TOOCAN across tropical regions
124 during this nine-year period.

Deep convective mask from collocated radar measurements

126 IR-only data from geostationary satellites are limited to the detection of cloud-top characteristics and do
127 not provide direct information on the internal processes, vertical structure, or dynamical evolution of
128 deep convection. Therefore**,** a comprehensive understanding of DCS dynamics requires the integration of
129 external datasets that capture precipitation, vertical cloud structure, and convective properties. By
130 combining geostationary IR observations with spaceborne radar measurements from TRMM-PR and GPM-
131 DPR, we can document not only the cold cloud shield but also the underlying deep convective processes
132 that govern the organization and life cycle of DCSs. However, while geostationary satellites provide
133 continuous monitoring of a given region, the low Earth orbit satellites TRMM and GPM offer only
134 instantaneous observations of specific regions as they pass over. A precise collocation procedure is then
135 required to integrate these datasets effectively.

136 In this study, we use Level-2 (L2) precipitation products from TRMM 2APR version 9 (V9) and GPM 2ADPR
137 version 07 (V07)**,** covering 2012–2013 (TRMM) (Kummerow et al. 2000) and 2014–2020 (GPM)
138 (Skofronick-Jackson et al. 2017) within the 30°S–30°N region. Both datasets have identical spatial
139 resolutions, with a 245 km swath width and a 5.1 km horizontal resolution. The vertical detection range
140 extends from the surface to 20 km**,** with a 0.125 km vertical resolution across 176 levels**.** ~~To~~In order to
141 ensure continuity, harmonization of TRMM-PR and GPM Ku-band (13.6 GHz) calibration has been carried
142 out, reducing systematic differences and improving long-term precipitation estimates. These efforts have
143 led to a fully inter-calibrated and homogenized radar database**,** ensuring consistency across the 9-year
144 (2012–2020) record for the tropical belt (Stocker et al. (2018), Ji et al 2022). For our analysis, we focus on
145 the classification of precipitation type into ~~convective and stratiform, (~~stratiform, convective and other
146 rain type, retrieved from the 2A23 algorithm (Awaka et al. 2009, Le and Chandrasekar 2013, Awaka et al.,
147 2016, 2021; Chen et al., 2025).

148 The first step of the ~~colocation~~collocation procedure involves selecting, for a given geostationary
149 platform, the IR images that can be temporally collocated with a particular TRMM-PR or GPM-DPR orbit.
150 Next, a spatial ~~colocation~~collocation procedure assigns geostationary IR pixels to spaceborne radar pixels.
151 Only geostationary pixels identified as DCSs by the TOOCAN algorithm are retained for further analysis.
152 Since the homogenized GEOring dataset and TRMM-PR/GPM-DPR have different horizontal resolutions,
153 we identify all GEO IR pixels that fall within the TRMM-PR and GPM-DPR footprints to ensure a proper
154 match. A temporal collocation step is also necessary, considering the time-scanning characteristics of each
155 geostationary platform (Fiolleau and Roca 2020). To ensure the quality of our analyses, only geostationary
156 pixels collocated with radar observations within a 15-minute temporal window are retained. This ensures
157 that the matched IR and radar pixels remain as temporally aligned as possible.

158 DCSs identified by TOOCAN and sampled by TRMM and GPM radars are re-mapped onto the TRMM/GPM
159 geo-referential frame, ensuring that their morphological characteristics (e.g., size, lifetime, eccentricity…)
160 are analyzed within the same spatial and temporal reference as the radar data. This alignment allows for
161 a more consistent and accurate comparison of DCS properties across datasets. The brightness
162 temperatures from geostationary satellites are also averaged to match the TRMM/GPM radar footprint
163 resolution**.**

164 By combining these datasets, we establish a coherent framework that integrates convective cold cloud
165 shields identified from TOOCAN and GEOring IR data, with precipitation-related processes from radar
166 measurements. More than 900,000 DCSs have then been sampled by TRMM and GPM orbit at one or
167 multiple stages of their life cycle, but not at every time step, due to the intermittent nature of radar
168 overpasses. For our study, restricted to tropical ocean over a more restricted latitudinal band of 25°S-
169 25°N, only DCSs with at least 70% of their cloud shield sampled by TRMM or GPM radar orbit (≈225,000
170 DCSs) are retained **(**Fiolleau and Roca, 2013b). This selection criterion ensures sufficient spatial coverage
171 and enhances the statistical reliability of the dataset, allowing a more comprehensive and representative
172 characterization of DCS properties throughout their evolution.

173 Tropical cyclones that could bias the DCSs' properties were removed by discarding any DCS whose
174 centroid lay within 250 km of an IbTrACS storm track (Knapp et al., 2010), after collocating the tracks with
175 TOOCAN algorithm (Fiolleau & Roca, 2024). Following previous classification studies, we kept only cloud
176 systems with lifetimes longer than 5 h and a well-defined life cycle, corresponding to Class 2a in Roca et
177 al. (2017). Emphasis is placed on the convection that occurs on the first half of systems' life cycle (Elsaesser
178 et al. 2022), thus the analysis is further limited to snapshots between 10 % and 50 % of each DCS's
179 ~~normalised~~normalized life cycle. Over the study period this screening yielded ≈60 000 co-located DCSs in
180 the TRMM-PR/GPM-DPR radar dataset. Hereafter, this dataset will be called the TOOCAN-radar dataset.
181 ~~Their~~The convective footprints of these collocated DCSs were delineated as illustrated in Fig. 1, which
182 shows a snapshot of a convective system detected by TOOCAN coincident with a PR/DPR overpass. Within
183 the radar swath, precipitation is classified as stratiform, convective, or non-precipitating~~; convective~~
184 following the precipitation type from the 2A23 algorithm introduced before, and excluding the "other"
185 rain type. Convective echoes are highlighted in red in Fig. 1.

186

187

188
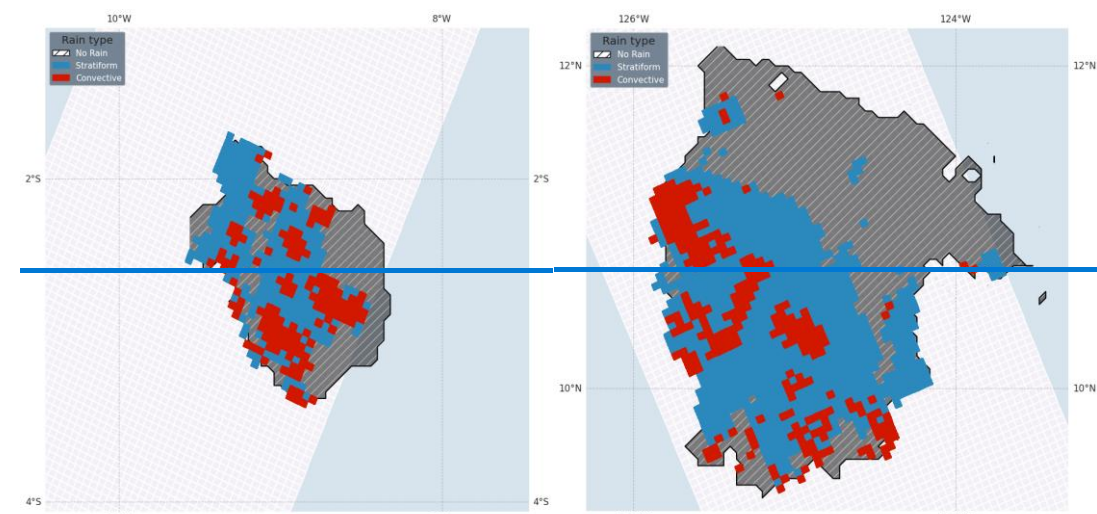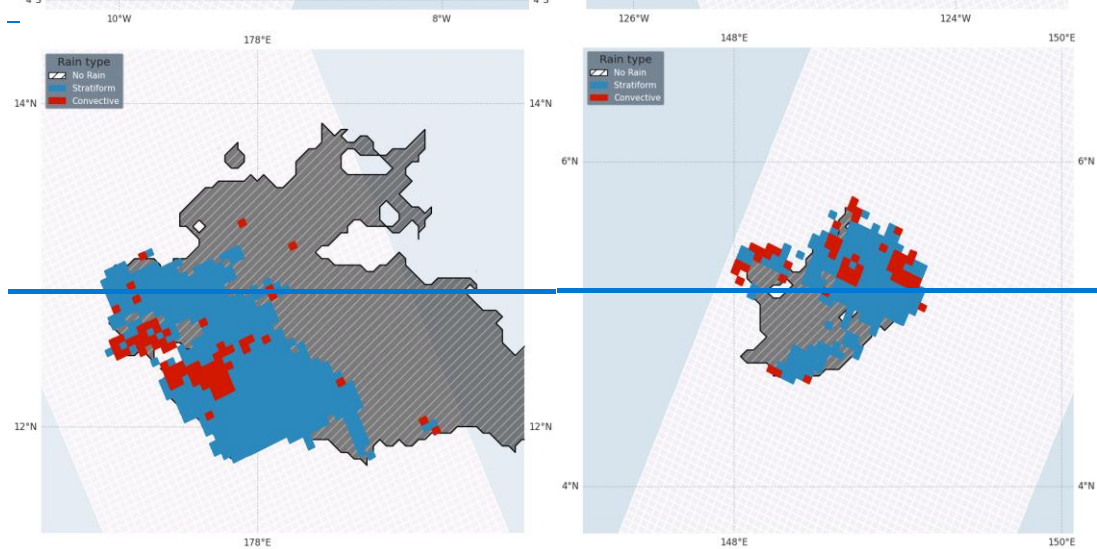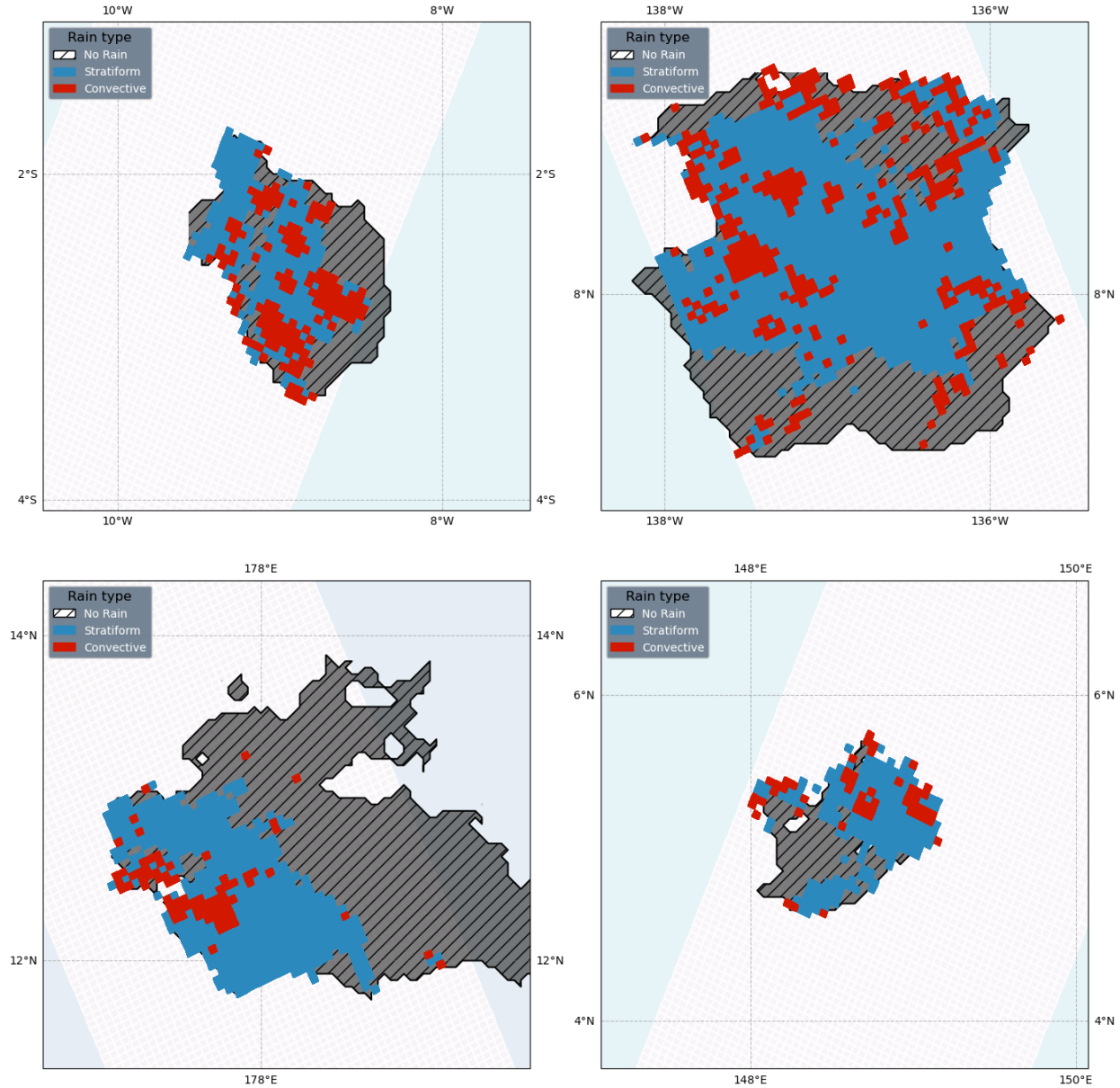
189 *Figure 1: Several examples from the TOOCAN-radar dataset. The TRMM/GPM swath along the track is*
190 *shown in white, while the TOOCAN cloud shield at the time of ~~colocation~~collocation is represented in*
191 *shaded-hatched grey. Different types of precipitation are displayed in color, with convective areas*
192 *highlighted in red.*

193 **2.2 Idealized model simulation**

194 The SAM model and the RCEMIP protocol

195 The cloud-resolving model System for Atmospheric Modeling (SAM) version 6.11.2 (Khairoutdinov &
196 Randall 2003) is used. The simulation follows the RCEMIP protocol for CRM with a 300K SST (Wing et al.,
197 2018) in a long channel configuration (6144x384km). The integration lasts 100 days and the last 25 days
198 only are used and analyzed here to remove spin-up effects (Wing et al., 2020). The resolution is 3 km in
199 both horizontal directions, and increases with height from a few tens of meters in the planetary boundary
200 layer to 500 m in the mid and upper troposphere. All integrations are performed ~~as per~~following the

201 original protocol with a specific output frequency of 30min instead of 1-3h and ~~the use of~~by using
202 instantaneous fields ~~instead of~~rather than hourly ~~averaged~~averages in order to permit the identification
203 and tracking of convective systems in this simulation.

204 To identify and track DCSs in the SAM simulation, the TOOCAN algorithm has been adapted to operate on
205 Outgoing Longwave Radiation (OLR) fields instead of traditional infrared brightness temperature (Tb)
206 imagery. While the core methodology of TOOCAN, based on spatio-temporal segmentation and iterative
207 thresholding, was preserved, the detection thresholds were defined to match the radiative properties of
208 the simulated convection. The initial convective seed detection was performed at an outgoing longwave
209 radiation (OLR) threshold of 73.90 W/m². The iterative region-growing process then expanded the
210 identified seeds using a 10-connected spatiotemporal operator, progressively including warmer
211 surrounding pixels up to a final threshold of 172.94 W/m², which corresponds to the upper boundary of
212 the cold cloud shield. This value is approximately equivalent to 235 K, following the Stefan–Boltzmann law
213 under the assumption of blackbody radiation. This adaptation enabled a consistent and physically
214 meaningful identification of DCSs in the high-temporal-resolution model OLR output.

215 Prior to applying the TOOCAN algorithm, a two-dimensional wrapping strategy was implemented to
216 ensure continuity in DCS tracking across the cyclic boundaries of the SAM domain. In the X-direction, the
217 domain was extended by duplicating the last 1500 km (corresponding to the final 500 grid points) and
218 appending it to the start of each OLR image. Similarly, the first 1500 km (first 500 grid points) were
219 duplicated and appended to the end. This symmetrical extension allows TOOCAN to detect convective
220 systems that traverse the zonal boundary without artificial segmentation. In the Y-direction, the entire
221 OLR image was duplicated and appended above and below the original field, effectively extending the
222 domain by 384 km in the meridional direction on each side. This ensures that vertically extended
223 convective systems near the Y-boundaries are also tracked without discontinuity. Following this wrapping,
224 any DCSs that were identified twice, once on each side of the duplicated X or Y boundaries, were carefully
225 merged or removed during post-processing to prevent double-counting in the final DCS database. This
226 approach ensures that the segmentation and tracking of DCSs are free from artefacts related to the
227 periodic geometry of the SAM simulation, enabling a reliable characterization of convective organization
228 across the full domain. Over the run period and 3 122 DCS have been identified in the simulation dataset.

Convection mask
230 While convection is typically identified in cloud-resolving models using a simple diagnostic, such as vertical
231 velocity exceeding 1 m/s at a given altitude (Varble et al., 2014), a more sophisticated method is employed
232 here. Specifically, a classification approach is employed to distinguish between convective, stratiform, and
233 cirriform regions within the cold cloud shield. The method is based on a simplified implementation of the
234 physical threshold technique (Marinescu et al., 2016). It relies on a combination of surface precipitation,
235 profiles of vertical velocity and cloud top information to identify the cloud type using various thresholds
236 outlined in Table 1. A grid box is classified as cirriform if surface precipitation is below the stratiform
237 precipitation threshold and OLR is colder than a specific threshold, corresponding approximately to an
238 equivalent brightness temperature of 235K. A grid box is classified as convective if the surface
239 precipitation exceeds the prescribed convective precipitation threshold. Alternatively, it can be also
240 classified as convective if the absolute value of vertical velocity updraft (or downdraft) above (below) the
241 0°C isotherm ~~exceeds the updraft threshold or falls below the downdraft threshold.~~exceed 5 m/s (3m/s).

242 Grid boxes that do not meet the criteria for either convective or cirriform classification are designated as
243 stratiform.

Convective Precipitation threshold (mm/h)	0°C isotherm height (m)	Cloud top height (m)	stratiform Precipitation threshold (mm/h)	Cirriform OLR threshold (Wm-2)	Updraft threshold above the 0°C isotherm (m/s)	Downdrafts ~~threshold~~Threshold below the 0°C isotherm (m/s)
10	3000	6000	0.04	172	~~3~~5	-~~5~~3

244 *Table1 the physical threshold used for convective/stratiform/cirriform classification*

245 Hereafter, the TOOCAN-RCE dataset refers to the data introduced in this section. Examples from the RCE
246 dataset are shown in Figure 2, sharing a similar layout and ~~colour~~color scheme than in Figure 1. Convective
247 and stratiform precipitation are rendered in red and blue, respectively. The convective echoes appear as
248 clustered patches whose boundaries are occasionally irregular.

249

250
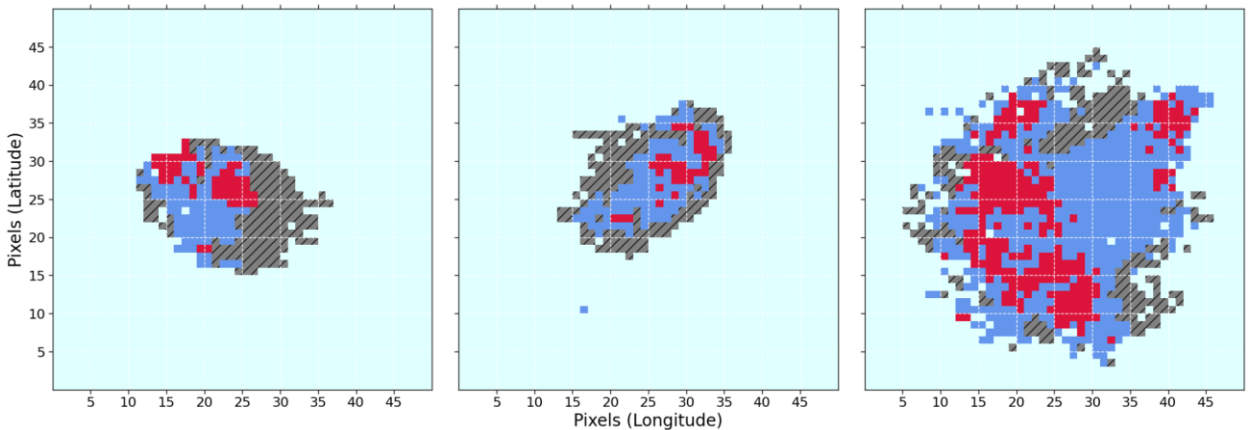
251 *Figure 2: Three illustrations of precipitation classification from the TOOCAN-RCE dataset, taken at a*
252 *selected time during the simulation within a 50x50 grid centered around the identified DCS. The TOOCAN*
253 *cloud shield is represented in shaded hatched grey. Different types of precipitation are displayed in color,*
254 *with blue indicating stratiform precipitation while convective areas are highlighted in red. The*
255 *~~idealised~~idealized ocean is colored in light blue.*

From convection mask to convective core identification and decomposition into elementary structures

257 The concept of convective cores from radar observations has been popularized in the 1970's thanks to
258 the GATE field campaign that was dedicated to deep convective systems in the tropical Atlantic Ocean
259 (Houze & Betts, 1981). Surface based radar indeed revealed echo structures in cloud systems that
260 exhibited a strong coherency in space and time and intensity. The radar is sensitive to the hydrometeors
261 distribution that results from vertical movements so that there is a physical, although not direct, link
262 between the radar echoes and the underlying convective updrafts and downdrafts (Houze, 1997). Detailed
263 analysis of the radar echoes further indicate that the intensity of the reflected radar power is indeed

stronger at the center of the echo compared to its edge. This "core" structure mimics well its dynamical
equivalent where convective vertical velocity exhibits more intense value at their core since the updrafts
there are preserved from entraining less buoyant environmental air. The vertical extent of the cores can
reach up to the tropopause for the deepest ones and their spatial extension spans a wide range from 1 to
15 km for the deepest convective one (López, 1978). When extended to space borne radar, similar
features are observed. Based on earlier investigations, Houze et al. (2007) and Romatschake et al. (2010)
propose to define a convective core as a 4-connected (by shared edges) cluster of high intensity radar
pixels (5km). Such Houze-like cores, depending on the thresholds used, can span a wide range of spatial
scales, from 5 to 100 km. The physical and dynamical interpretation depends upon the size of the object
and some of its vertical characteristics and encompasses not only deep convection but a large spectrum
of convective activity and remains somehow qualitative (Chen et al., 2025; Houze et al., 2015). Figure 3
(left) presents a sample of radar measurements in which convective pixels are identified in red (see
Section 2, Data). Six convective cores have been labelled in Figure 3 (middle) using the Houze-like
clustering technique. These cores exhibit a range of sizes, from as small as 1 pixel to as large as 30 pixels—
approximately 150 km² for the green core.
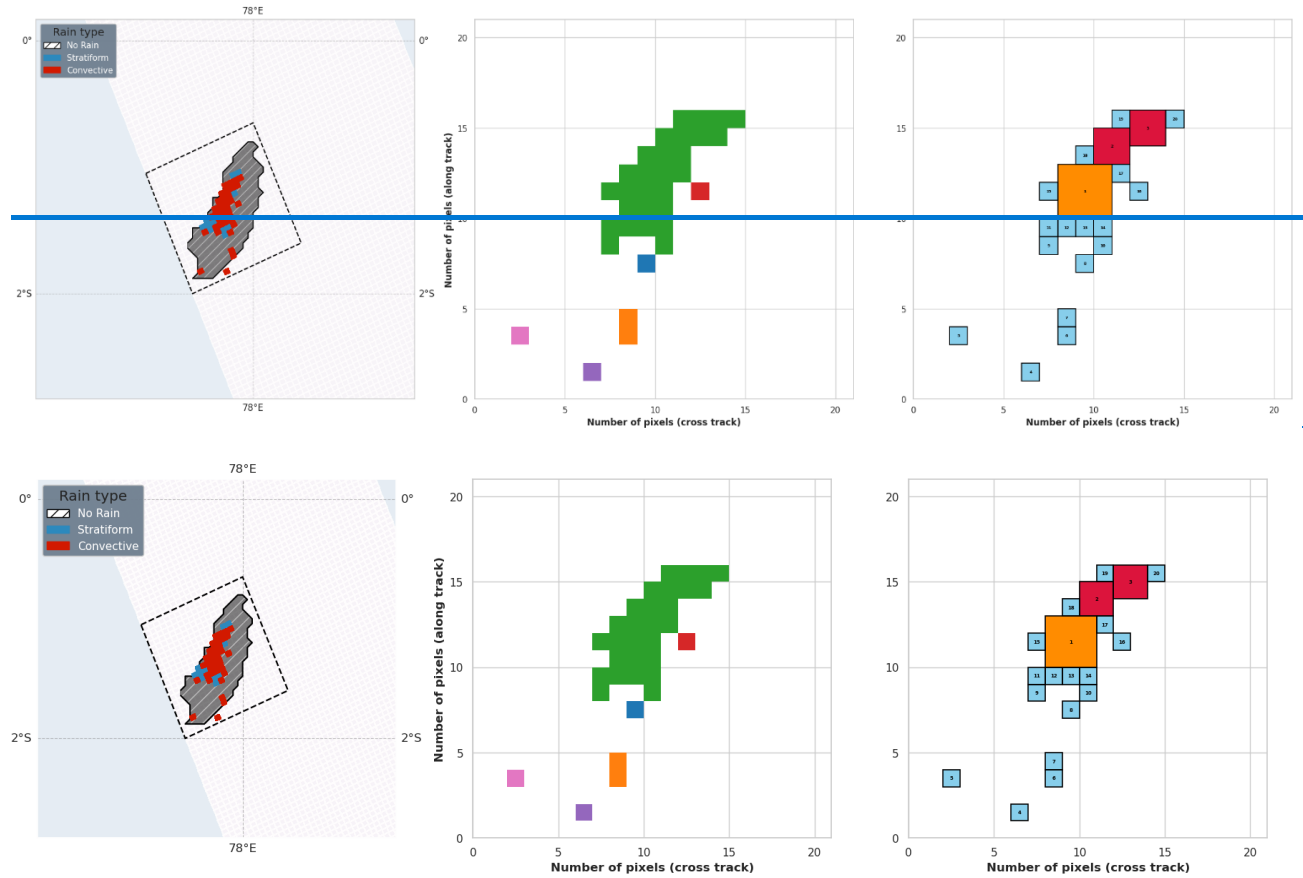
*Figure 3: Left: Same as figure 1 for another satellite scene, the black-dashed contour showing the
rectangular area that encompasses the cloud shield and defining the scene extent. Middle: basic 2D
segmentation of the convective field within the scene with shared edges, each entity is represented by a
color. Right: decomposition into basic square structures by decreasing size, each structure is represented
by a color and a number that is the edge length of the square.*

286 To move beyond this qualitative framework, we propose a finer-scale decomposition of the clustered echo
287 regions into elementary convective structures. This approach relies on the assumption that the spatially
288 continuous distribution of hydrometeors, and consequently of radar reflectivity, arises from aggregated
289 finer scale underlying dynamics. This approach can be viewed as an upscaled, space-borne version of the
290 analysis of precipitation core and updrafts/downdrafts joint occurrence analysis from high-resolution
291 ground-based observations (e.g., Moroda et al., 2021; Lamer et al., 2023). In this perspective, we assume
292 that the large cluster of continuous echoes (colored in green in Figure 3, middle) is composed of smaller
293 coherent and compact convective features akin to a circular bulk updraft of varying diameter that we
294 approximate using size varying squares. ~~This approach can be seen as an upscaled, space borne version of~~
295 ~~the high-resolution precipitation ground based core and updrafts/downdrafts joint occurrence analysis~~
296 We hence add a morphological constraint to the classical core segmentation. ~~(e.g., Moroda et al., 2021;~~
297 ~~Lamer et al., 2023).~~

298 The decomposition technique is further detailed in Annex A. An example of the decomposition is shown
299 in Figure 3 (right) where the 30-pixel central core, as identified by the Houze-like methodology, is now
300 broken down into 13 single pixel elements, two 2x2 pixels elements and one 3x3 pixels element. In this
301 example, the maximum size of square elementary structure (MaxSquareSize) that fits in the convective
302 mask is 3 (Figure 3 middle). Our decomposition technique, as well as the Houze-like clustering technique
303 have been applied on the TOOCAN-radar and TOOCAN-RCE datasets. The core size distribution confirms
304 the difference between Houze-like clusters and the results from the decomposition ~~in~~into elementary
305 square structures (Figure 4). For the TOOCAN-radar dataset, the Houze-like cores are log-linearly
306 distributed with a maximum size up to 17x17 pixels equivalent (roughly 7200 km²) while the present
307 decomposition prevents clusters larger than 9x9 pixels, roughly 2000km2 (Figure 4, left).

308
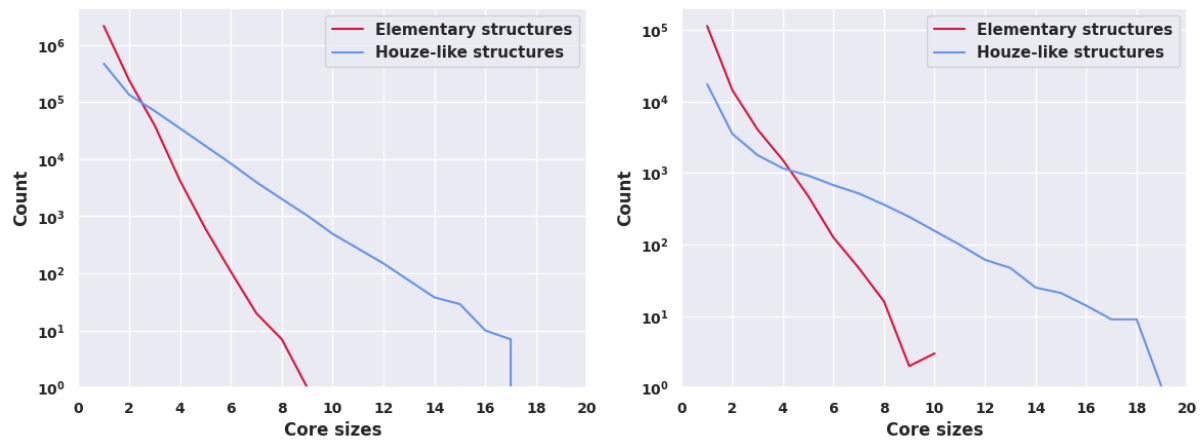
309 *Figure 4: Size distribution of the convective cores Left: TOOCAN-radar dataset. Right: TOOCAN-RCE*
310 *dataset. The Houze-like detection is* ~~*represented in blue*~~*shown in blue and corresponds to the rounded*
311 *integer value of the square root of the cores' area, while our elementary decomposition is shown in red*
312 *and corresponds to the size of the square cores.*

313 Similarly, to the radar observations, km-scale model simulations can be analyzed in terms of elementary
314 structures. While resolving the deep convective updrafts/downdrafts dynamics requires hectometric
315 resolution (Bryan et al., 2003), km-scale models have been shown to produce reasonable vertical
316 velocities and precipitation structures (Kukulies et al., 2024). At these spatial resolutions, though, the

317 updrafts/downdrafts correspond more to a bulk plume associated with a coherent hydrometeors loading
318 across a few grid points (Varble et al., 2014) , similar to what is observed in the radar data. As exemplified
319 in the next section, our technique successfully decomposes the convective mask from the simulations (see
320 section Data above) into elementary structures like the one illustrated in Figure 3 (middle). Statistically,
321 differences similar to the radar case hold for the TOOCAN-RCE dataset (Figure 4, right) with elementary
322 structures reaching maximum size up to 10x10 grid points, roughly 900km2.

323 In both datasets, the detection of the convective cores thanks to the decomposition in elementary
324 structures prevents the building of very large patches of convection that are delicate to interpret
325 physically. While a thorough exploration of the better dynamical and physical consistency of the present
326 core identification compared to a simple 4-connectivity segmentation is deferred to future work, Figure 5
327 shows a comparison of the mean vertical profile of reflectivity for the present decomposition is compared
328 to and that of Houze-like cores in Figure 5, using 8 years of collocated radar measurements to allow for
329 robust statistics. The present decomposition reflectivity shows a pattern similar for all cores sizes. It is
330 composed of an almost constant distribution from surface up to the freezing level (≈5km) and then a
331 slowly decreasing reflectivity up to the maximum altitude of deep convective reflectivity typical of deep
332 convective structures (e.g., Zipser et al. 1994). This pattern scales well with the size of the core, showing
333 well discriminated profiles as the size increases. Houze-like cores, in contrast, show overall weaker mean
334 reflectivities. Also, the Houze-like profiles exhibit much less variation with the size of the core than the
335 present decomposition. The stronger reflectivity of the present decomposition, for a given size, suggests
336 more homogenous profiles being aggregated together resulting in the enhanced mean profile compared
337 to Houze-like cores. The two decompositions also differ in how well they resolve size-dependent physics.
338 In the elementary-structure case, the altitude of the 30 dBZ isosurface rises steadily from ≈ 4 km for 2×2
339 cores to ≈ 9 km for 8×8 cores, , indicating that larger structures are associated with stronger and deeper
340 convection (Fig. 5, left). Houze-like cores smaller than 6×6 never reach 30 dBZ, and larger ones show no
341 clear trend (Fig. 5, right). Similar comparisons using the simulation's vertical velocities confirms the lack
342 of coherency of the large patches from the Houze-like segmentation (not shown).

343

344
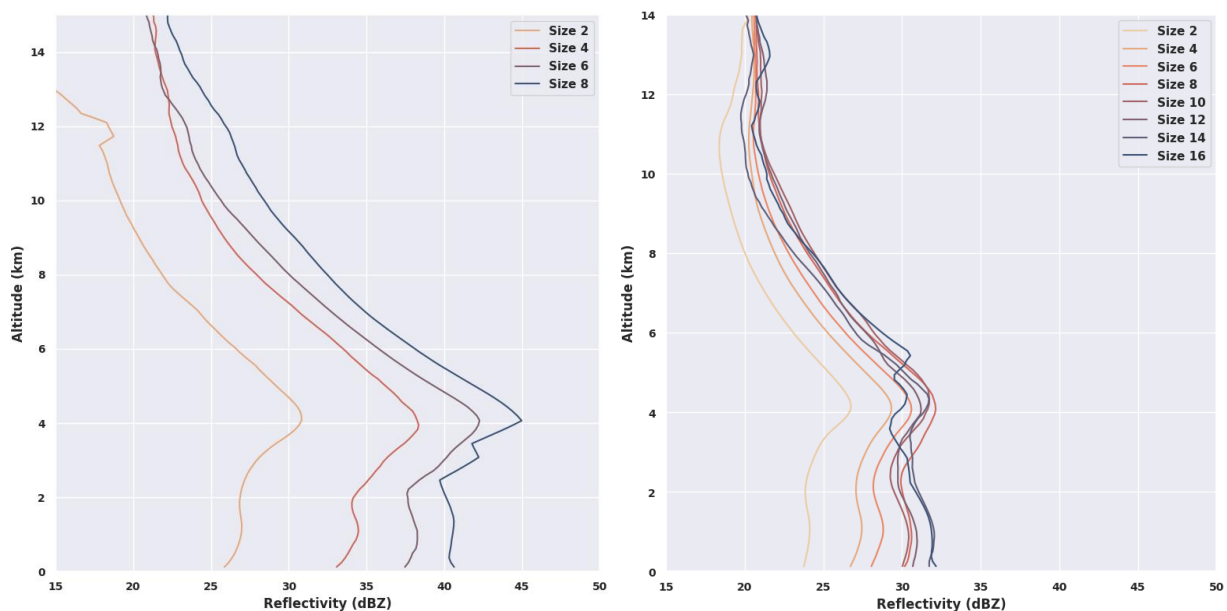
Figure 5: Reflectivity profiles (composites using 8 years of collocated radar measurements) of convective ~~core~~cores for Left: our elementary decomposition, Right: Houze-like shared edges decomposition, with different core sizes shown in color.

We acknowledge that this decomposition relies on strong assumptions about the underlying dynamics behind the radar echoes or model convective mask clusters. Nevertheless, the present effort is one step toward improving the consistency between the core identification and the underlying dynamical object. As demonstrated in the next section, this approach significantly enhances the characterization of the organization of convection within the cloud shield of DCSs.

3 The method

3.1 Rationale

The aim is to classify a scene based on the spatial arrangement of the convective cores within the convective system's cloud shield. The cloud shields span a wide diversity of scales and shape (Roca et al. 2017) and the density of convection across the shield also exhibit large variations (e.g., Elsaesser et al., 2022). As a consequence, unlike regular gridded data of fixed size, the method ~~is required~~requires defining a selected area that corresponds to ~~be shield-specific~~the cloudshield dimensions. To address this requirement, we qualify the spatial arrangement of convection in the cloud shield by comparing the actual scene with an ensemble of generated scenes for which the spatial arrangement of the cores is randomly distributed in the shield. The generated scenes have the same characteristics as the actual scene in terms of convective fraction, distribution of the size of the cores, and differ only by the spatial arrangement of the cores. This measure of a deviation from a random state is inspired from i) the work of Koren et al. 2024 where they applied their methodology to a 2D cloud mask within a selected area, ii) the organization irregularity index (OII) from Biagioli et Tompkins 2023 that is a function of the distribution's departure from randomness across the full spectrum of spatial scales. This stochastic approach allows for the ~~computation~~estimation of the probability that a given arrangement of convective cores could arise purely by chance. This ~~probability~~metric, together with the characteristics of the scene (see dedicated part in section 3.2) forms a small set of key ~~variables~~parameters (Janssens et al. 2021) that are used to characterize the organization of convection using an unsupervised simple classification procedure. In the following, the algorithm and its domain of applicability are presented in detail.

3.2 The algorithm
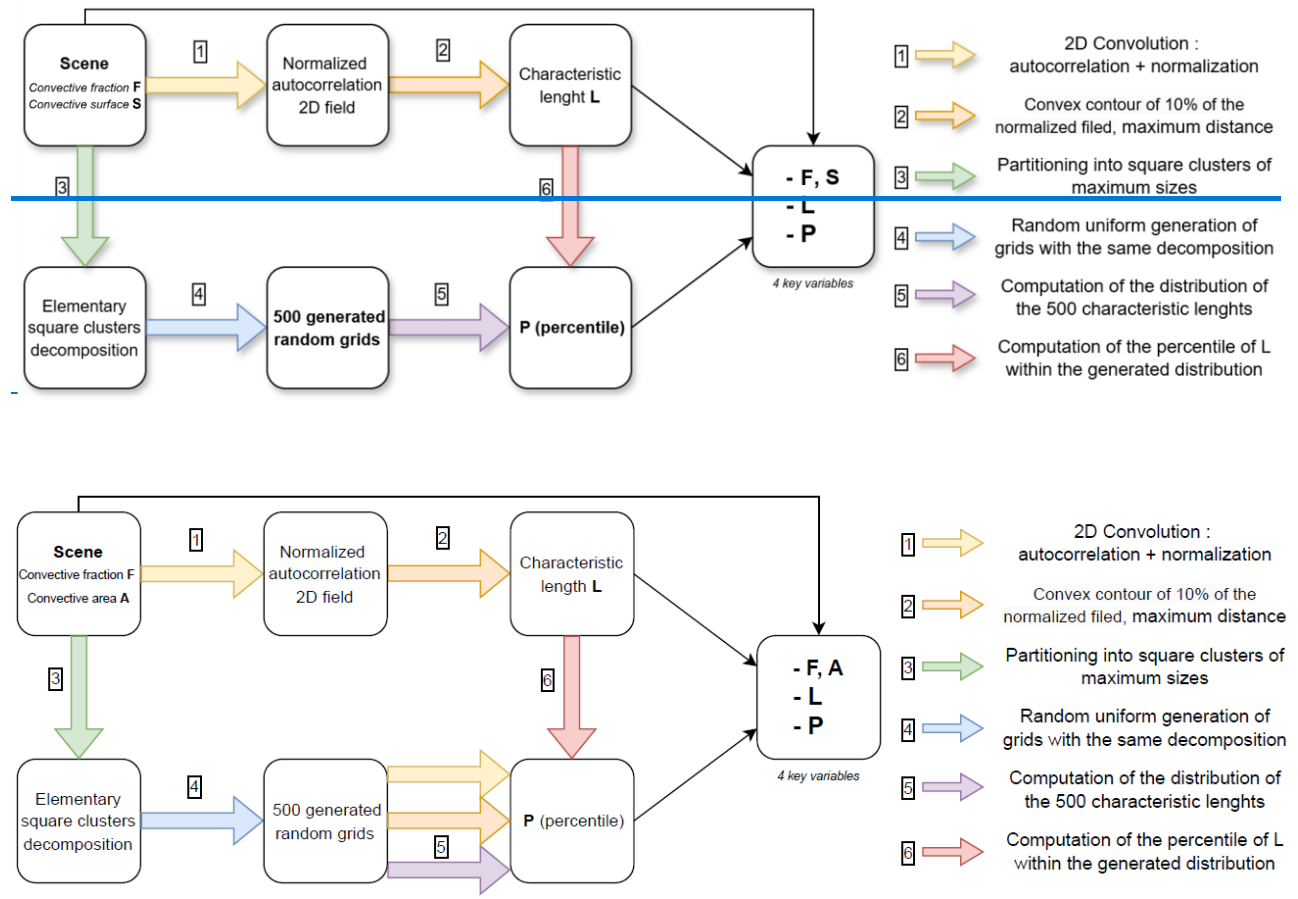
Figure 6: Overview of the algorithm to compute the 4 key ~~variables~~parameters of a scene.

Figure 6 shows the structure of the algorithm used to derive the 4 key ~~variables~~parameters corresponding to a given scene. The following sections describe each step of the procedure and details the computations that are represented by the colored arrows in Figure 6.

Scene characterization

Definition

A scene is defined as the rectangular area that encompasses the cloud shield identified by the TOOCAN algorithm, as illustrated by the black contour in Figure 3 (left). Assuming the individual pixel area is similar across the grid, the total surface of the scene is expressed in pixels. ~~Four variables to quantify the organization will be introduced below.~~ We introduce four ~~variables~~parameters to quantify convective organization. The first two parameters describe ~~how convection is distributed across the scene, whereas the last two characterize the spatial arrangement of the convective cores for a fixed~~ the amount of convection within the scene, using both absolute and relative metrics.

Convective ~~surface S~~area A and convective fraction F

The convective ~~surface S~~area A corresponds to the number of convective pixels in the scene. The convective fraction F is the proportion of those pixels regarding the area of the scene and is expressed in percent (upper-left box of figure 6).

Characteristic length of convection arrangement in the scene

A characteristic length scale is computed to summarize the macroscopic spatial coherence of convection within the scene. It is defined as the maximum distance between any two pixels in the spectrally transformed version of the scene. This metric will later be used to compare the observed scene with the corresponding generated one.

The length L is hence obtained by applying various filters on the scene (upper line workflow in Figure 6). The 2D autocorrelation spectral power field of the scene is computed and normalized (yellow arrow in Figure 6). The 2D autocorrelation power is illustrated in Figure 7 (and Figure S1) for two typical scenes selected from the satellite dataset. The compactness of the scene shown in the top panel, is expressed by a strongly marked central area in the 2D power map, while the second scene, in the bottom panel displays a more spread feature indicative of lower spatial autocorrelation. Although two-dimensional autocorrelation and Fourier analysis are mathematically related, we ~~favour~~favor autocorrelation because it is less sensitive to the noise and spurious features that commonly appear in convective fields (Figures 1 and 2).

The first filter, applied on to the normalized spectral power field, is a simple threshold of 10% to delineate the region of interest within the scene. Only the central shape is considered hereafter (Figure 7, bottom-right). To handle the rare cases for which this contour would exhibit complex, twisted, or distorted shapes, the smallest convex contour that encloses it, is identified (blue contour in Figure 7). The characteristic length L is finally obtained as the maximum distance between any two pixels inside the convex contour (orange arrow in Figure 6).

416

417
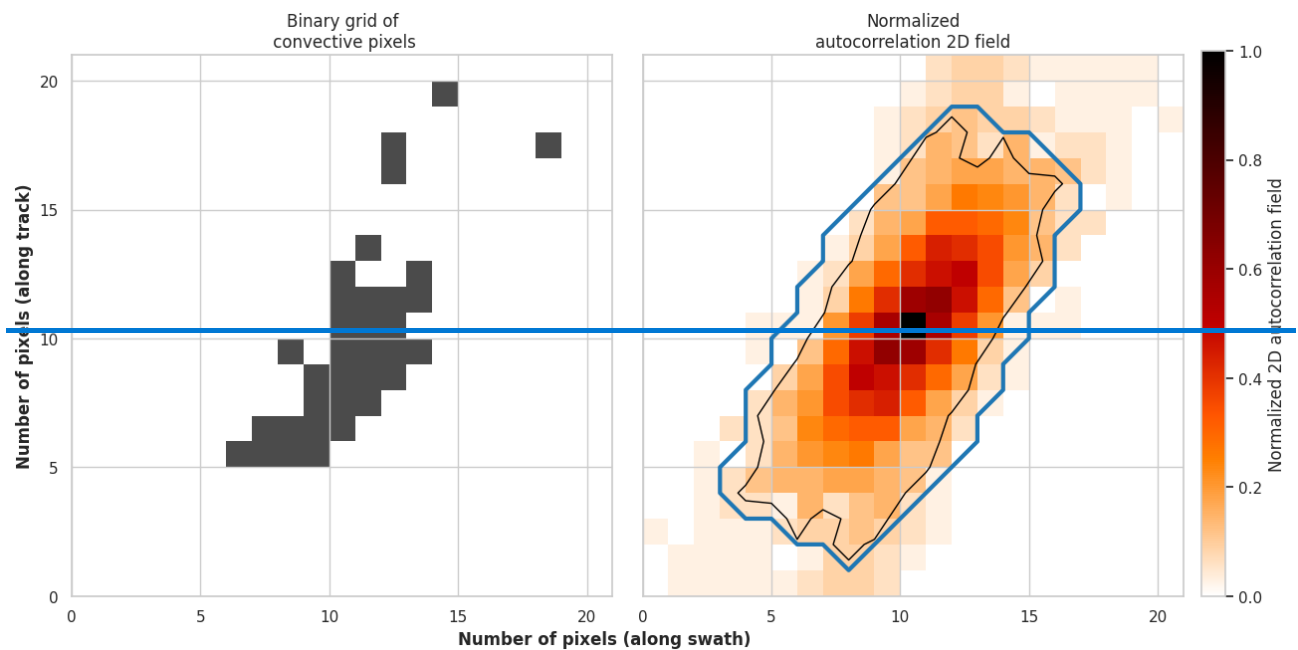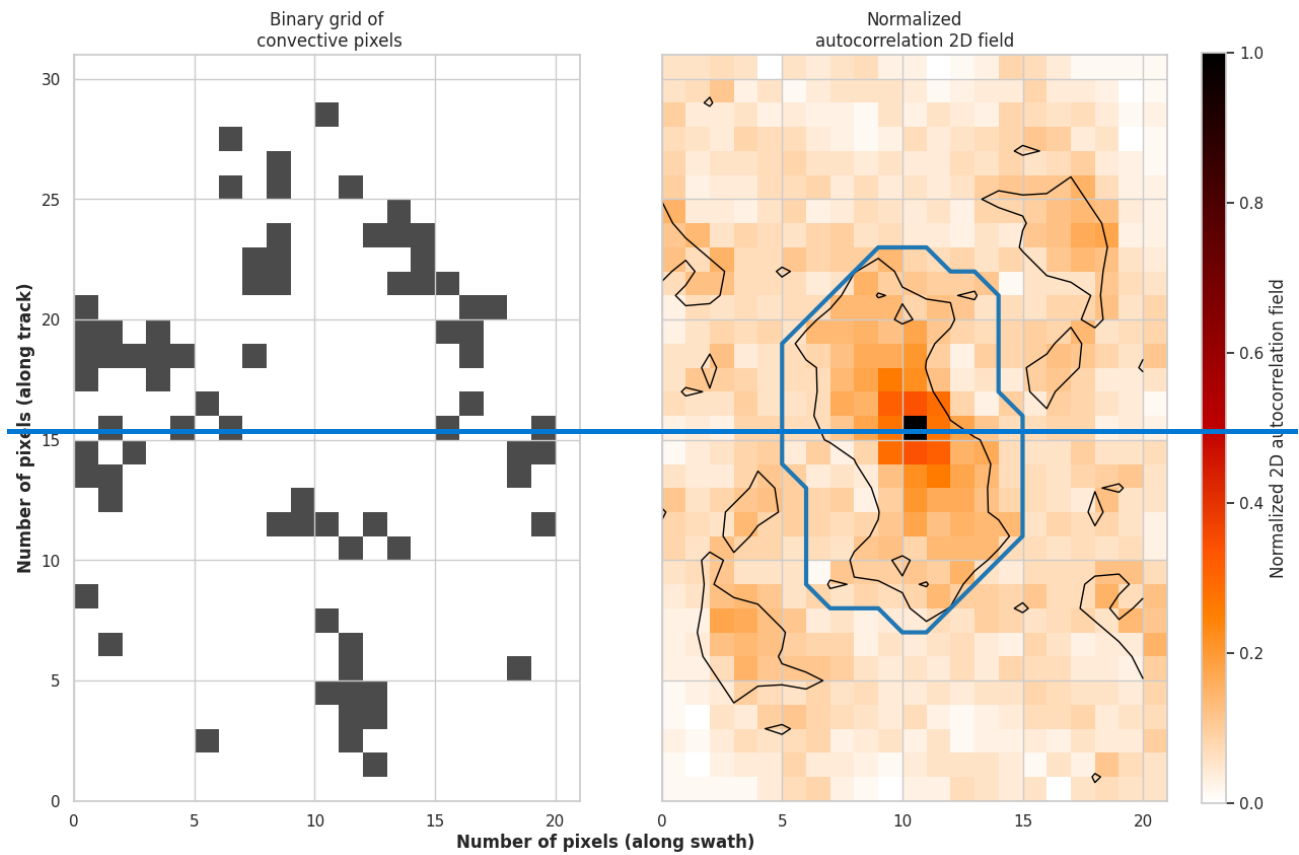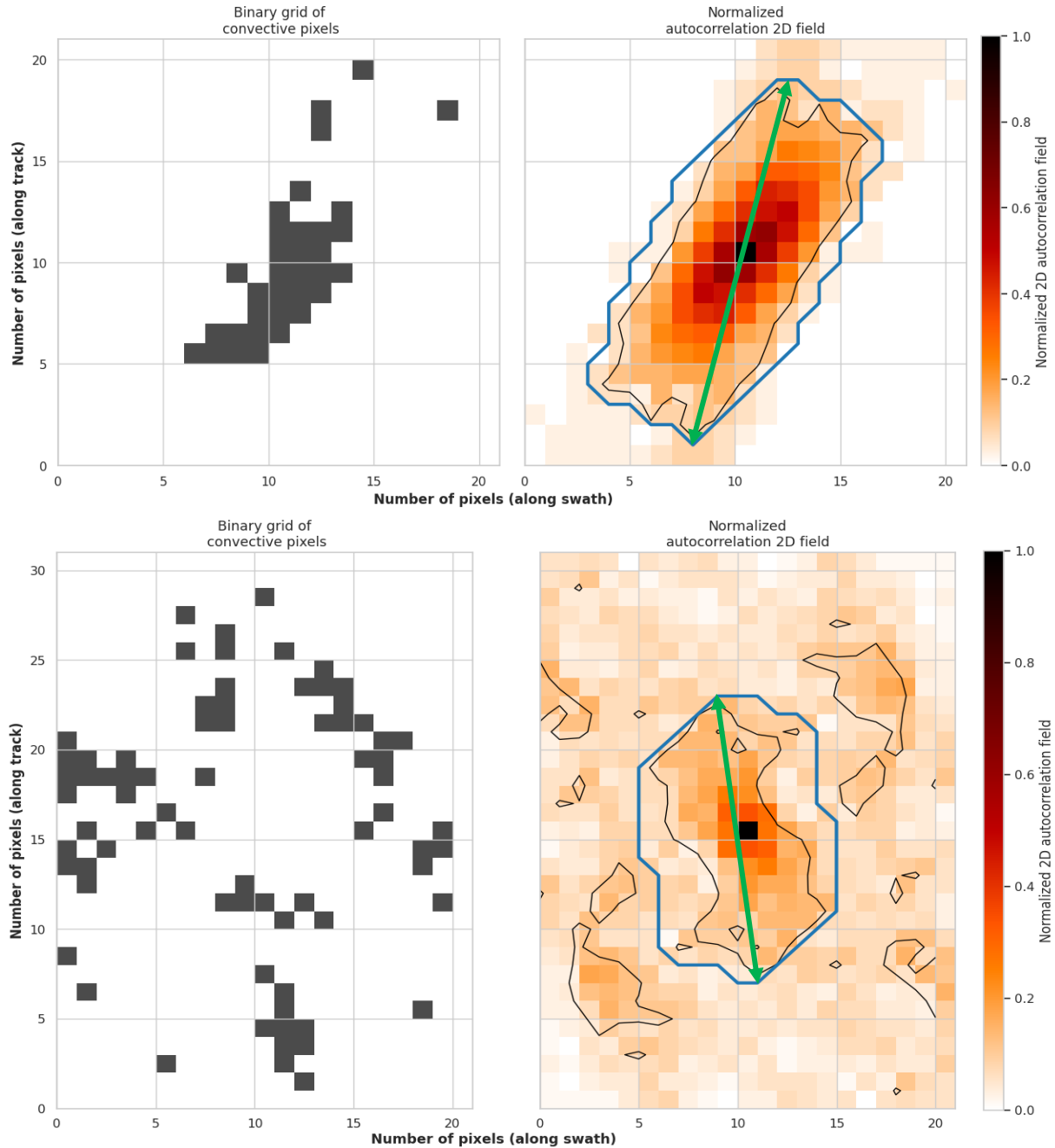
Figure 7: *Two selected scenes within the TOOCAN-radar dataset. Top: More compact convective field,*
Bottom: More spread convective field. Left: 2D binary scene (black pixels represent convective areas).
Right: 2D autocorrelation normalized field, black contour shows the 10% contour and blue contour
represents the convex contour that encompasses that 10% contour. The characteristic length L is the
maximum distance between 2 points within the blue contour, *represented with the green arrow,* *here*
top: L≈18.44, bottom: L≈14.~~14~~94 (pixel unit~~)~~).

This isocontour, ~~centred~~centered on the peak of the power map, delineates the spatial extent where
spatial correlation remains significant. It marks the threshold beyond which structural repetition becomes

426 negligible, thereby providing a measure of the decorrelation scale, e.g., the characteristic distance at
427 which recurring motifs lose coherence. The contour's shape reflects anisotropy. A near-circular form
428 indicates isotropy with uniform repetition in all directions, while elongated or asymmetrical contours
429 reveal directional dependence. Its size quantifies how spatially spread the pattern is within the image and
430 results from a balance between spatial arrangement and overall convective fraction F within the grid.
431 Other examples of this process using the 2D autocorrelation fields are shown in Figure S1 (supplementary
432 materials).

433 The extraction of L is performed in the 2D autocorrelation space, rather than directly from the raw
434 convective field. As a result, L encodes both the perception of the spatial morphologyextent of the main
435 structures of the raw field and the condensed structural information regarding the spatial arrangement
436 of these structures captured by the autocorrelation. However, the signal-to-noise ratio and the area of
437 validity of this 2D field must be carefully assessed to ensure a reliable interpretation of the L values as
438 defined here. Sensitivity to the arbitrarily selected threshold and limits of applicability are further
439 discussed in Section 3.2.4 and in Annex B.

440 C and SA are two of the 4 key variablesparameters to characterize a scene and are independent from the
441 relative spatial organizationarrangement of the cores. They contain information on the overall filling of
442 convective structures within the cloud shield, while the variableparameter L contains information on the
443 organization for given F and SA. The L scale will be ultimately compared to that derived from stochastic
444 modelling, including scene generation, to calculate the probability for the scene being randomly organized
445 or nota percentile-based measure of deviation from randomness.

446 Scenes generation
447 In this section, the stochastic approach is described, along with the definition of the fourth key variable,
448 P, the probabilityparameter, P, that represents a percentile-based measure of the scene's spatial
449 arrangement to deviate from a random distribution (lower line workflow in Figure 6). The decomposition
450 in elementary structure is first performed (See Section 2 and Annex A, green arrow in Figure 6) and used
451 in a bootstrapping step to generate an ensemble of scenesMonte-Carlo approach for generating a
452 reference distribution under spatial randomness (blue arrow in Figure 6).

453 *Bootstrapping*
454 Monte-Carlo approach

455 The geometric properties of the scene, such as its size, convective fraction F, and the cores from the
456 decomposition into elementary structures, are used to generate synthetic scenes, in which the segmented
457 cores are randomly distributed in space following a uniform distribution. This approach is conceptually
458 similar to that of Haerter et al. (2019), who also used a uniform law to position the centers of "cold pools"
459 in fixed grid sizes. Importantly, the original convective fraction F and convective surface Sarea A of the
460 convective cores are preserved in each generated synthetic scene, only their spatial arrangement differs.
461 Figure 8 illustrates the procedure: from the scene (a), the elementary decomposition is performed (b) and
462 two generations of the same core's partition are randomly displayed (c, d). The first realization results in
463 low L values, while the second, where the largest cores are more spatially clustered, yields higher L values.
464 This demonstrates that in some cases, random distribution can produce spatial arrangements that are
465 comparable in terms of L values, to that of the original scene.

466 An ensemble of 500 synthetic scenes, for satisfying statistical robustness (see Annex B), is generated and
467 for each of them, the characteristic scale L is computed as described previously. Thus, a synthetic
468 distribution of random surrogates of the original scene has been created and the L distribution of these
469 random scenes is assessed (Figure 9, purple arrow in Figure 6). This distribution serves as a reference for
470 evaluating the degree of spatial ~~organization~~arrangement in the identified scene relative to the generated
471 ensemble.

472
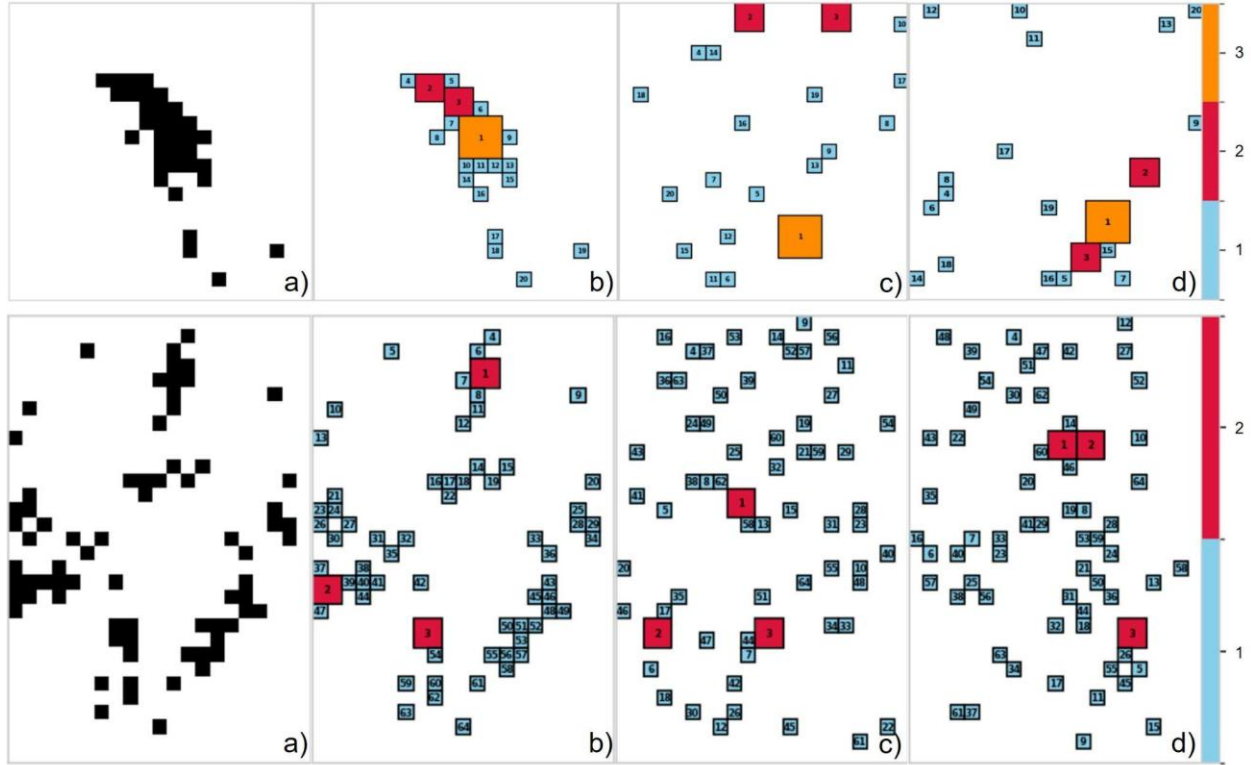
Figure 8: a) 2D binary scenes as shown in Figure 7. b) elementary decomposition into square clusters.
(c,d) : Generated scenes with the same number of square clusters, randomly and uniformly distributed,
the c/d panels are respectively a scattered/clustered random positioning that produces lower/higher L
value.
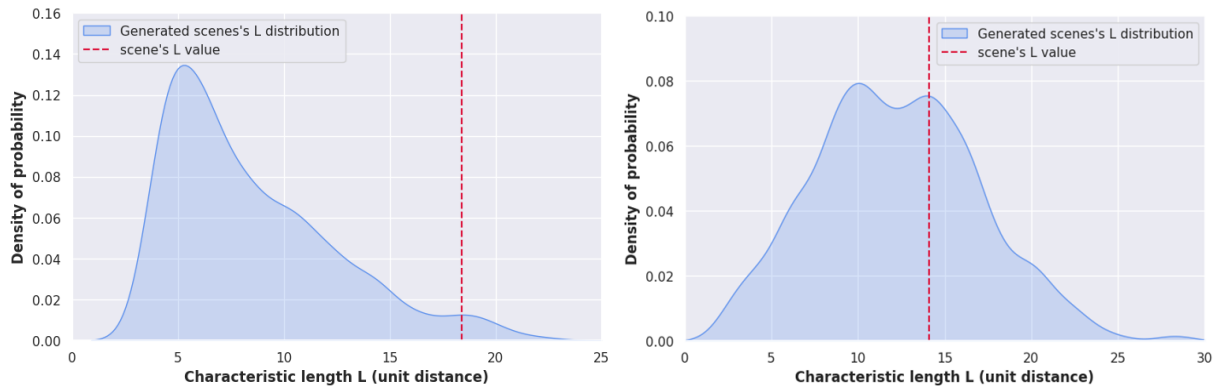
478 *Figure 9: Left: (respectively right) Empirical probability density function (estimated via KDE) of the*
479 *generated distribution of characteristic length L for the scenes in Figure 7, top (resp. bottom). The scene's*
480 *L value is represented with a vertical dotted red line.*

481 *Computation of P*
482 The comparison of the identified scene to the ensemble of generated length scales L is performed by
483 computing ~~the probability of the occurrence~~a percentile P, which quantifies the deviation of the real
484 scene's spatial arrangement from a random arrangement (Figure 9, Red arrow in Figure 6). This
485 ~~probability~~measure is estimated by computing the percentile of the scene's L within the generated
486 distribution. For instance, a value of P = 0.1 indicates that 450 out of the 500 generated random scenes
487 have an L value greater than that of the real scene. Conversely, a value close to 1 means that almost no
488 randomly generated scenes produce a characteristic length L greater or equal than the one from the
489 scene. This implies that such a specific spatial arrangement (or its equivalent) almost never occurs in the
490 randomly generated scenes. The combination of P with the 3 other ~~variables~~parameters provides a fully
491 comprehensive characterization of the complexity of the spatial arrangement for a given scene (Figure 6).

Limits of applicability
493 In some cases, the quantification of spatial arrangement of convection is an ill-posed problem and
494 provides little if any insights into the underlying physics. This happens when the scene has obvious
495 limitations in size or convective fraction. It can also arise from sensitivity of the stochastic model to some
496 of these characteristics of the scene. Indeed, the generation of the ensemble of scenes ~~with a~~given a
497 convective fraction (F) and convective area (A) is constrained by a few parameters of the stochastic model,
498 namely, the number of realizations, the threshold used for contour identification during the computation
499 as well as the maximum size of the elementary structure (MaxSquareSize). The sensitivity of F to the two
500 former parameters are discussed in Annex B while this section focuses here exclusively on the sensitivity
501 to MaxSquareSize, as it is the primary influencing factor.

502 Idealized simulations were carried out to estimate the variations in the distribution of length as a function
503 of the F ~~variable~~parameter and varying MaxSquareSize values. Using a fixed 50x50 pixels grid, the
504 distribution of length generated for a given F value and a selected MaxSquareSize are ~~analysed~~analyzed
505 to determine whether the ~~probability~~percentile of the L value of the scene could be accurately assessed.
506 The parameter MaxSquareSize has a significant impact on shaping the L distribution, as shown in Figure
507 10. The mean of L is an increasing function of F, as expected. However, the growth is non-linear.
508 Specifically, it becomes challenging to compute a meaningful ~~probability~~percentile when L values are
509 confined near 0 (e.g., for low F and MaxSquareSize = 1, as shown in Figure 10, left) or when L values
510 saturate at the grid's diagonal length, $(49^2+49^2)^{0.5} \approx 69.3$, which occurs for high F values and
511 MaxSquareSize ≥ 5 (Figure 10, right).

512
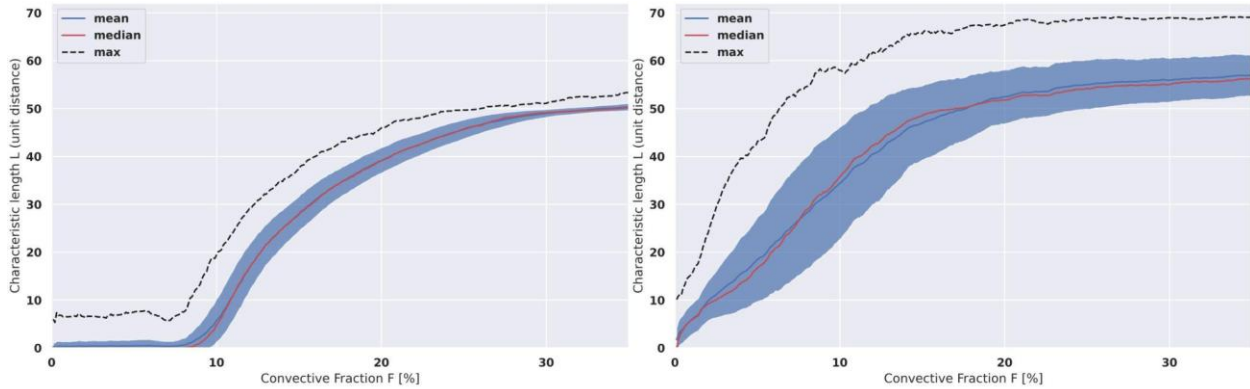
Figure 10: Characteristic length L plotted against convective fraction F. 500 generation of 50x50 grids for Left: only square clusters of size 1 (MaxSquareSize = 1), Right: same but for square clusters partitioned with MaxSquareSize <= 5. The red line indicates the median of the distribution, the dark blue line shows the mean and the dotted-black line represents the maximum value of L within the distribution. The shaded blue area represents +/- 1σ. The x-axis resolution is 0.1%, with a 1.5% rolling mean applied for readability.

Based on these diagnostics we limit the applicability of the algorithm to the scene whose convective fraction lies between two empirical bounds: Minimum convective fraction F_{min}(MaxSquareSize) = 8% for MaxSquareSize ≤ 1 and Maximum convective fraction F_{max}(MaxSquareSize) = 25% for MaxSquareSize ≥ 5. Scenes that do not satisfy these thresholds are discarded, guaranteeing that the subsequent characterisation remains physically meaningful and robust.

Data processing

A minimum ~~grid~~scene size criterion is also used to filter out scenes with less than 8×8 grid size and less than 5 convective pixels, as characterizing scenes below these thresholds provides limited insight into the spatial ~~organization~~arrangement of convective structures. Therefore, very small scenes or scenes containing sparse convective areas are not characterized. After applying those filtering, roughly 20% of the TOOCAN-radar dataset is filtered out. This number is down to 5% for the TOOCAN-RCE dataset. The final datasets then consist of 54 132 scenes for the TOOCAN-radar dataset and 2 941 scenes for the TOOCAN-RCE dataset. For each of these scenes, the four key ~~variables~~parameters are computed to characterize their spatial arrangement, which serves as the basis for the classification. Table 1 summarizes the baseline configuration used to perform these computations prior to the final classification step, while duration and maximal size distributions of DCSs selected in both datasets are shown in Figure 11. In both datasets, the population of DCS under consideration spans a wide range of morphology for short to long-lived and from small to very large systems confirming a good diversity of scenes for the analysis.

537

Threshold for convex hull identification	10%
Number of ~~bootstrap~~Monte-Carlo realizations M	500

Minimal grid size	8x8
Minimal total convective area S_{min}	6 pixels
Minimum convective fraction F_{min}(MaxSquareSize)	8% when MaxSquareSize ≤ 1
Maximum convective fraction F_{max}(MaxSquareSize)	25% when MaxSquareSize ≥ 5

538 *Table 2: baseline configuration.*

3.3 Results

Diversity of the scenes

More than 54000 and 2900 scenes are available for the TOOCAN-radar and TOOCAN-RCE datasets respectively. The morphology of the cloud shield of the DCS associated to these scenes is summarized in Figure 11. For both the TOOCAN-radar and TOOCAN-RCE datasets, the duration and maximum area (in km²) span a wide range of values consistent with the unfiltered distribution (not shown) suggesting that the population of scenes under analysis is representative of the DCS distribution.
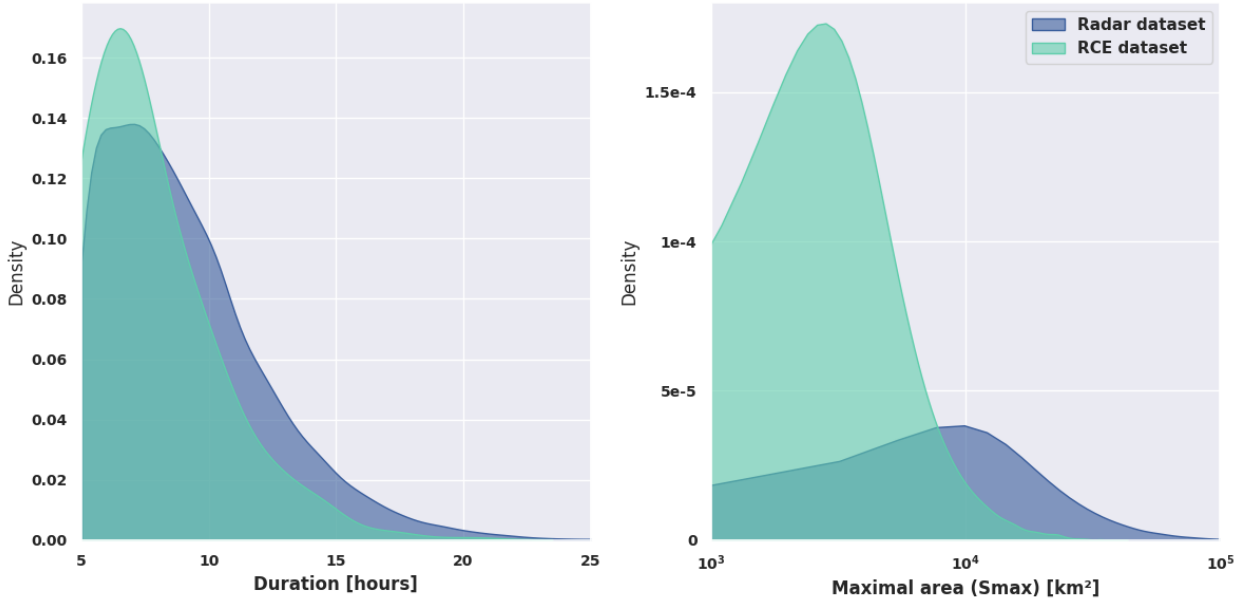
Figure 11: Empirical probability density function (estimated via KDE) of DCS properties from the scenes. Left: Duration in hour, Right: Maximum area in km² for the TOOCAN-radar dataset (dark blue) and the TOOCAN-RCE dataset (light blue).

The four key variables'parameters' distribution are shown in Figure 12, for both datasets. While the DCS and their internal organization from idealized simulations cannot be compared one-to-one with the TOOCAN-radar dataset, the similar distribution of F, SA, L and P suggests a very good behavior of the SAM model in simulating DCS. This point has already been noted either in global CRM configuration (Feng et al., 2025; Abramian et al., 2025 submitted) as well as in RCE configuration (Roca et al.,2024).

555 Figure 12 indicates that the convective fraction, size of convection area and characteristics lengths of the
556 scene of the datasets span a large range of values, with slightly skewed distributions. These distributions
557 are indicative of a wide diversity of spatial arrangement of convection in the scenes, both for the radar
558 and the simulation. On the other hand, the P distribution, indicating the probability of the characteristic
559 length to differ from a random arrangement (Figure 12, d) is very much skewed to the highest values
560 (around 1) with a very long tail. This indicates that only very few scenes can be associated with a randomly
561 generated pattern. The fact that the general features of these distributiondistributions are found in both
562 the TOOCAN-radar and the TOOCAN-RCE datasets further suggests that the use of the four parameters to
563 characterize the scenes allows to address the diversity of the convective organization, independently of
564 the marker used to identify convection, from the hydrometeors in the case of the radar and from the
565 vertical velocity for the simulation.

566

567
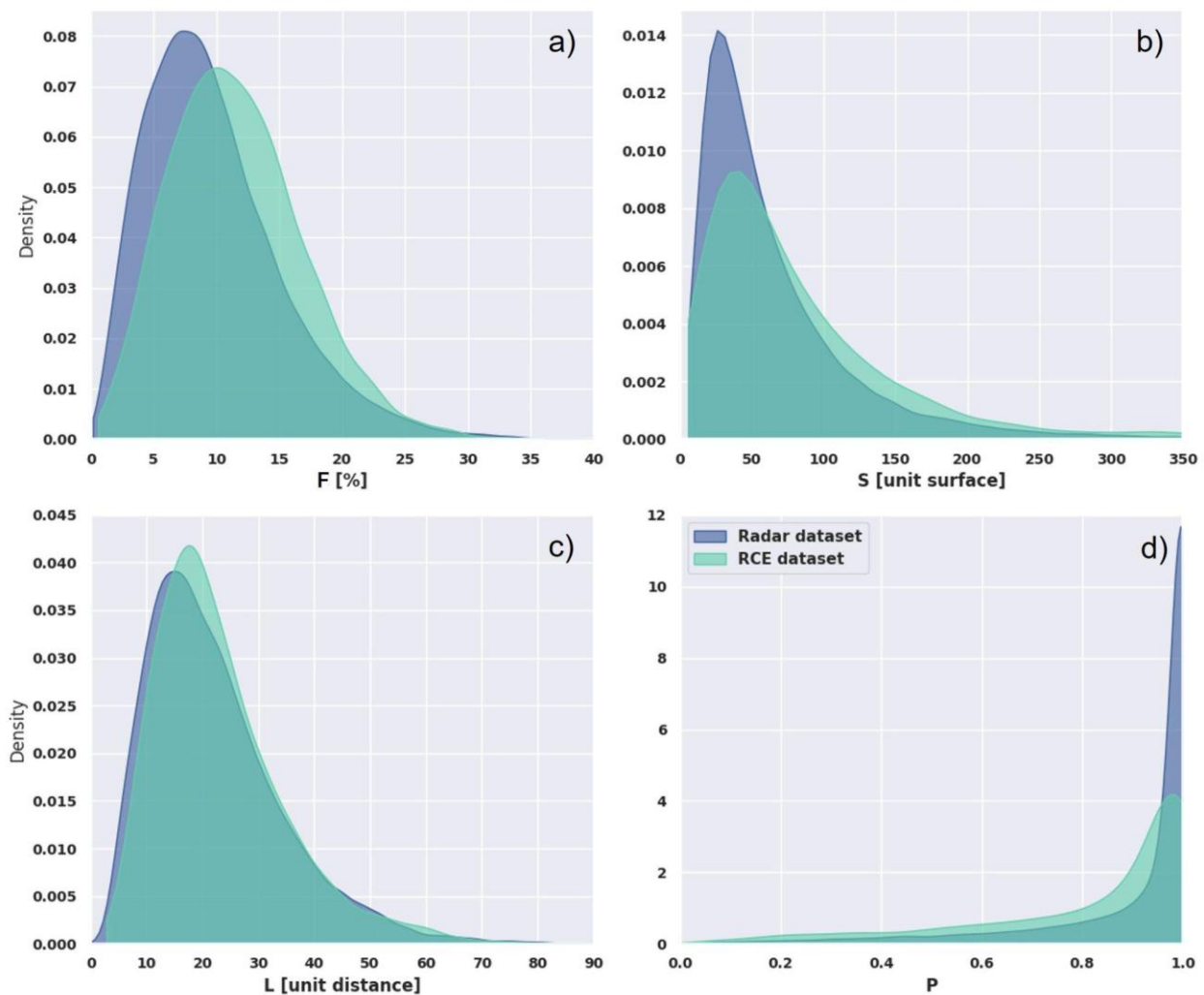
568 *Figure 12: Empirical probability density function (estimated via KDE) of the 4 key ~~variables~~parameters*
569 *within the TOOCAN-radar dataset (dark blue), the TOOCAN-RCE dataset (light blue). From Top to*
570 *Bottom, Left to Right~~: F, S, L and P~~: convective fraction (F), convective area (A), characteristic length (L)*
571 *and percentile (P).*

Organization of convection

The organization of convection can now be related to the multivariate coherency of our 4 parameters to characterize a scene. This 4-dimensional space is analyzed thanks to a simple unsupervised classification technique (K-mean). Four classes are hence automatically built for each of the datasets. ~~Empirical~~Classical clustering metrics (a trade-off between elbow and silhouette scores) show optimal results when separating the scenes into four classes. The results indeed reveal well separated classes, showing as separated pairs of distributions for each ~~variable~~parameter (Figure ~~12~~13). As shown in Figure 13 d and h, three of the classes are associated with the high values of P and one class stands out as possibly randomly arranged scenes, corresponding to the small occurrences of the long tail of the distribution (less than 20% see Figure S2).

582
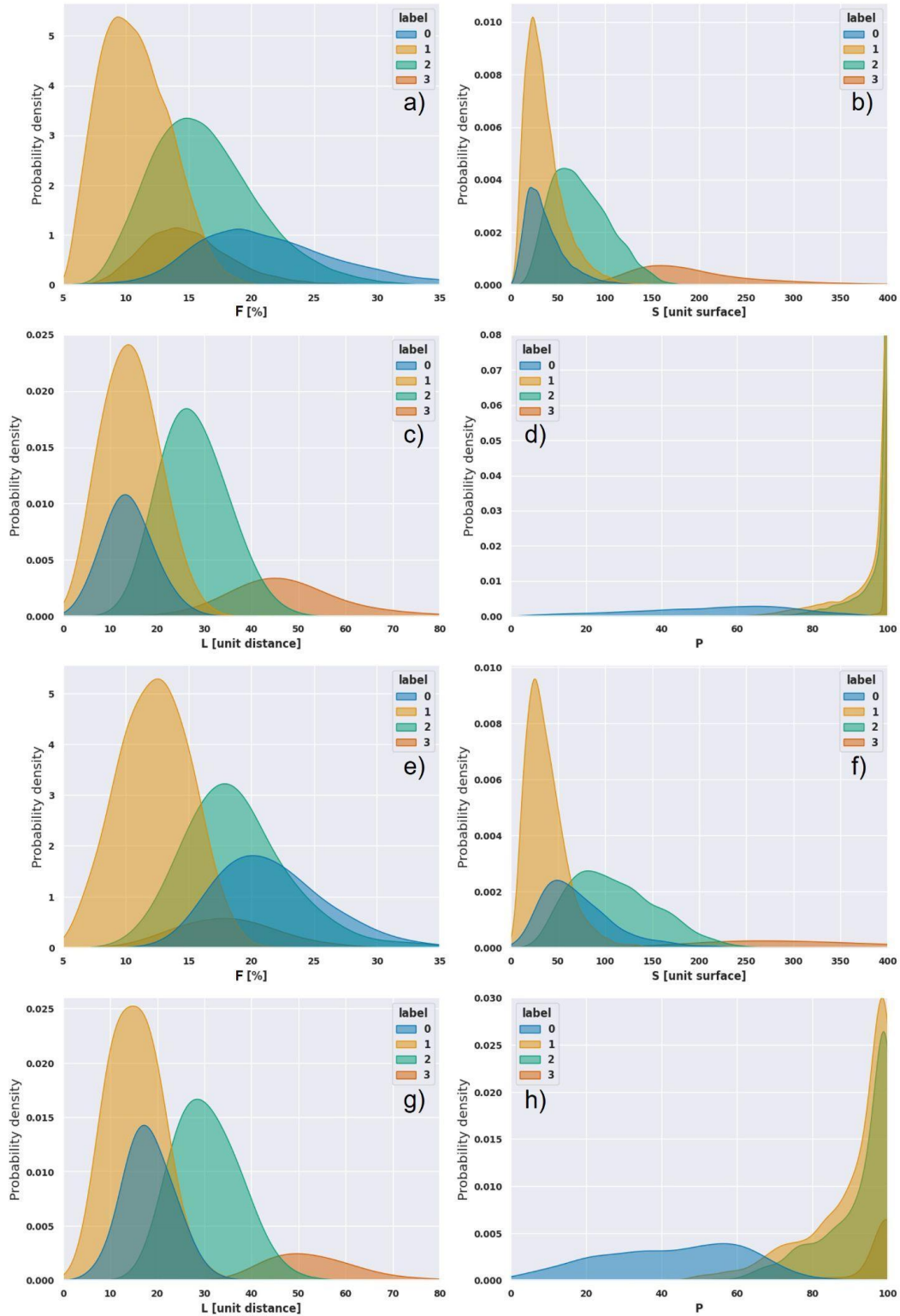
Figure 13: Empirical probability density function (estimated via KDE) for each class. Top: Convective scenes from the TOOCAN-radar dataset, Bottom: Convective scenes from the TOOCAN-RCE dataset. a, e) convective fraction F, b, f) Total convective area ~~S~~A (in pixels), c, g) Characteristic length L (in distance unit), d, h) ~~Probability~~Percentile P~~.~~

An increase in P, together and secondary with the variables L and A, corresponds to a higher level of organization. Accordingly, the classes are ordered from class 0, representing the least organized state, to class 3, representing the most structured. More specifically, class 0 (in blue) represents convective organizations that are ~~more randomly distributed~~the least clustered (characterized by relatively small L and P), even when F is high. In contrast, the class 3 (in dark orange) exhibits the most structured convective areas (high L, ~~S~~A, and P), despite relatively small F values. This indicates that F alone is not ~~a discriminating variable~~sufficient to fully discriminate between organization types, as the spatial arrangement strongly influences the other three key ~~variables~~parameters. Highly organized scenes (very unlikely to be randomly spatially ~~organized~~distributed with high L values) do not ~~necessarily~~ have high F values, as the dominant factor is the arrangement of the structures inside the cloud shield. In contrast, a clear relationship between L and ~~S~~A is observed, with both ~~variables~~parameters varying consistently across the four classes, as expected (Figure ~~12~~13). The primary distinction between the two intermediate classes lies less in their level of organization (both share similar P distributions) and more in the extent of the convective areas. Class 1 (in yellow) corresponds to scenes with relatively small convective areas (low F and ~~S~~A), leading to smaller L values compared to the class 2 (in green), which represents scenes with larger convective areas. The Class 0 and 3 represent the extreme opposites in terms of organization, and they are clearly separated in the ~~S~~A, L, and P spaces. The Class 0 scenes differ from the Class 1 primarily in F and P, while the Class 2 and 3 scenes are mainly distinguished by ~~S~~A and L. The least distinct separation occurs between class 1 and 2 scenes, as they only partially differ in F, ~~S~~A, and L. The Class 1 scenes systematically exhibit lower values than Class 2 for these ~~variables~~parameters, suggesting that these two organizational types are closely related. While Class 1 represents a less pronounced version of Class 2 in terms of convective area within the cloud shield, their spatial arrangement remains comparable, as indicated by their comparable P distributions. Finally, beyond a certain threshold of ~~S~~A (depending on the dataset), the scene can only be of Class 3 (Figure ~~11~~13). This means that the most structured type of organization always occurs once there is enough convective area within the scene. This also indicates that for the majority of ~~S~~A values, knowing the values of the two ~~variables~~parameters F and ~~S~~A is not enough to properly separate different types of organization. The overall classification is highly consistent across the two datasets, showing similar class distributions within the four-dimensional space and comparable general ~~behaviour~~behavior. Again, despite differences in ~~the~~ the marker used to identify convection, this suggests that our method gives rise to well separated classes to handle the diversity of scenes found in both datasets.

Figure 14 presents archetypal scenes from the TOOCAN-radar dataset for each class, selected by identifying the scene closest to the class centroid in the four-dimensional variable space. As expected, Class 0 displays a popcorn-like pattern characteristic of weakly sheared environments (e.g., Anber et al., 2014). Class 1 corresponds to a small system with a compact convective zone, while Class 2 exhibits a similar structure but on a larger spatial scale. Class 3 shows well-organized convection, exemplified here by a linearly structured convective system (e.g., Houze, 2004). Based on this classification, we propose the following class labels: Likely Random (label 0; blue), Clustered and Small (label 1; yellow), Clustered and Large (label 2; green), and Very Structured (label 3; dark orange). Their abbreviated names are LR, CS, CL, and VS, respectively.

The strong discriminating power, illustrated with this visual example (other examples for the TOOCAN-radar dataset can be found in Figure S3 and in Figure S4 for the simulation), of our method revealed here thanks to a basic unsupervised classification technique is the results of the selection of our 4 key parameters to characterize the scenes. These four features indeed contain enough information to

discriminate between random and organized spatial arrangement. In particular the detection of cores
thanks to the decomposition into elementary structures helps the quantification of the degree of
organization compared to a randomly distributed scenario.
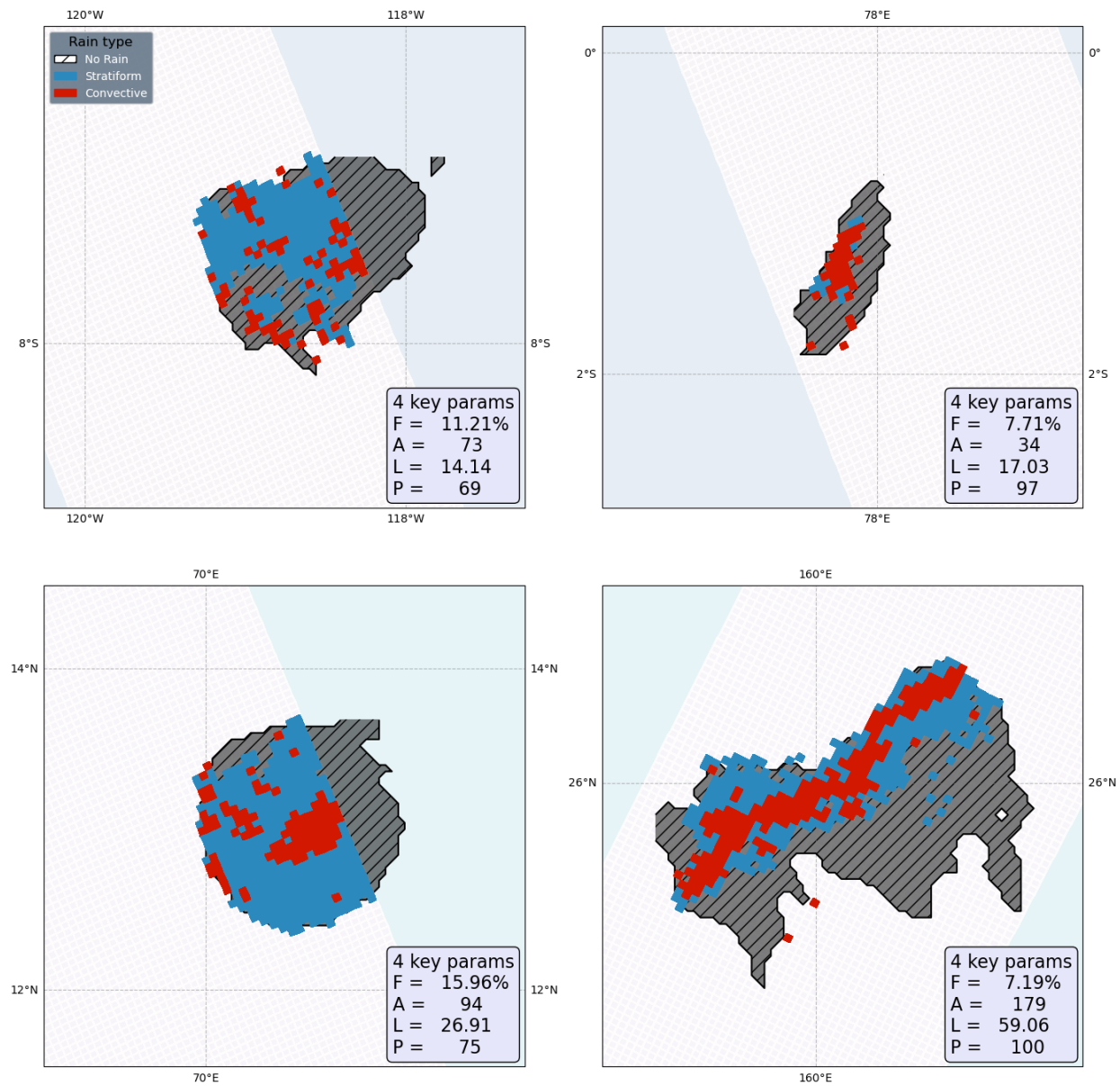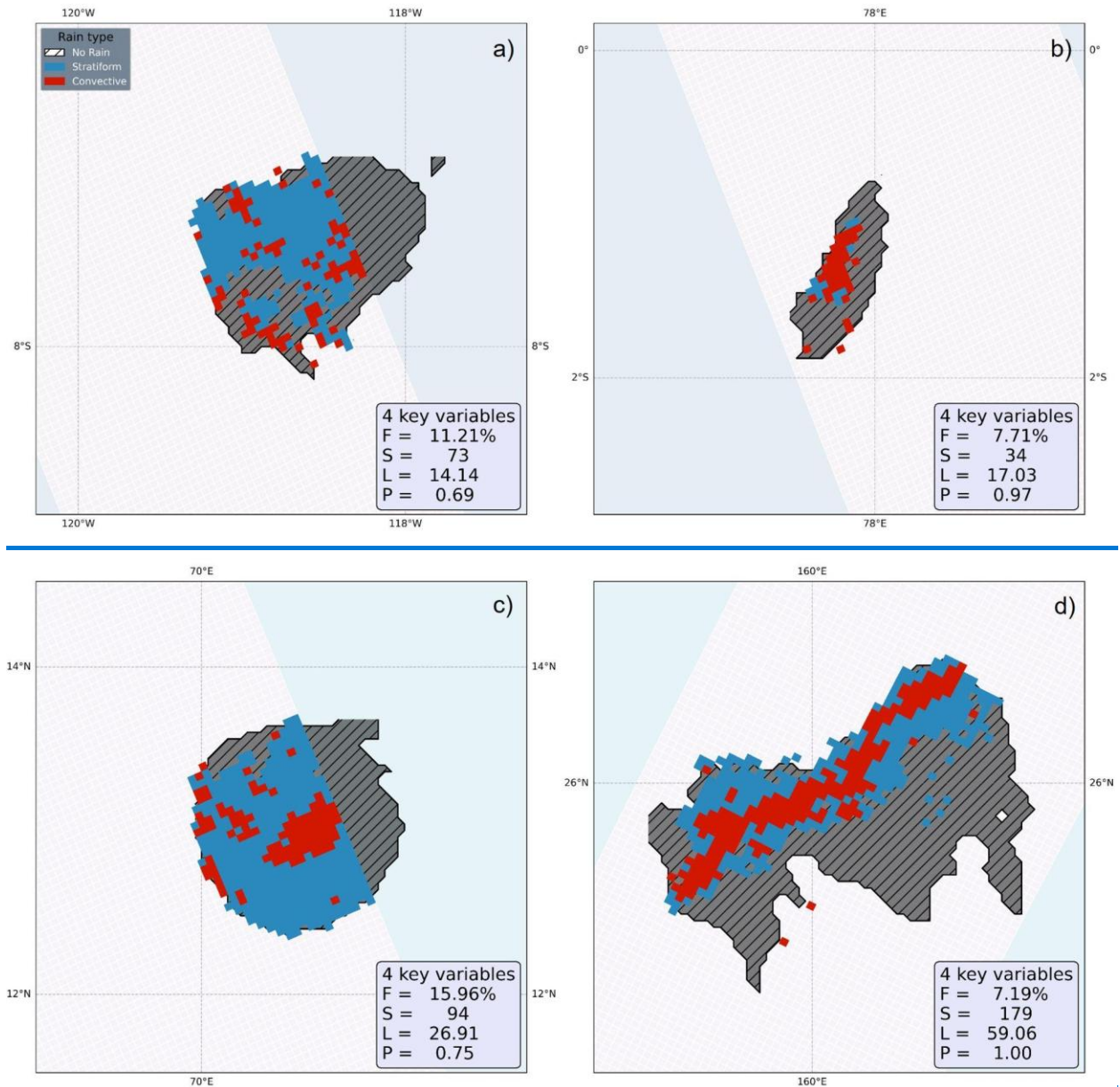
Figure 14: Same as figure 1. Archetypal examples of a) likely random (LR), b) clustered small (CS), c) clustered large (CL), d) very structured scenes (VS). The values of the four key ~~variables~~parameters are indicated for each example.

The reprojection of the four classes onto the morphological aspects of the associated DCSs is illustrated in Figure 15. As the level of organization increases from LR to VS, the distributions of these two morphological parameters shift towards higher values, reaching a maximum for the VS, which are predominant in the long tail (exceeding 20 hours and 80,000 km²). This finding indicates that the organization, as measured by this approach, plays a substantial role in shaping the morphology of the DCSs throughout their lifecycle.
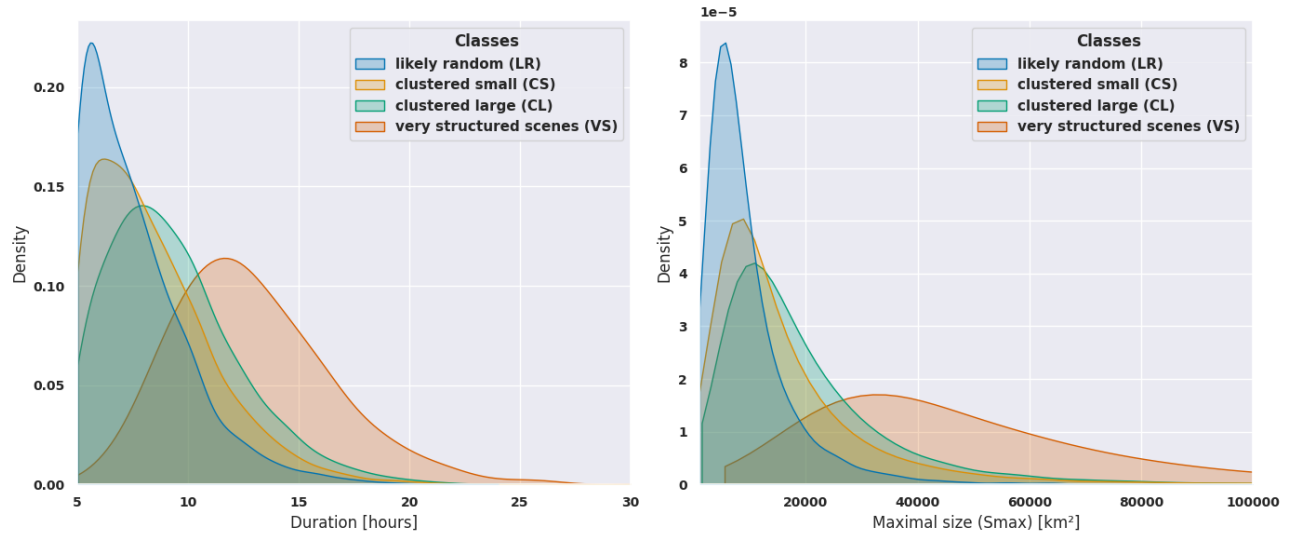
Figure 15: Empirical probability density function (estimated via KDE) for each class from the TOOCAN-radar dataset. Left: Duration (lifetime in hours), Right: Maximum extension of the associated anvil cloud along the life cycle of the DCS.

4 Discussion

The results above demonstrate that F and ~~S~~A alone, among the four ~~variables~~parameters, are insufficient to effectively distinguish between organizational classes, as they only partially capture the spatial arrangement of convection. To comprehensively characterize the diversity and complexity of spatial patterns, additional diagnostic measures are necessary. We therefore introduced the more elaborated ~~variables~~parameters L and P, which extend the analysis by incorporating both the spatial configuration of the elements and a estimation of the probability that the observed distribution deviates from randomness. These ~~variables~~parameters offer a more nuanced and robust understanding of spatial organization beyond what F and ~~S~~A can provide.

As stated in the introduction, a number of metrics have been introduced to quantify the organization of convection (Biagioli and Tompkins 2023, Mandorli et al. 2024). Their ability to discriminate between the scenes has been already questioned and is further assessed using our two datasets as a benchmark. The likely random (LR) and very structured (VS) classes are clearly identified in both datasets and correspond to distinctly different arrangements of convection and are hence used to perform this assessment. Three well-known metrics are compared to our 2 most contrasted classes in Figure ~~15~~16.

The first metric is the Convective Organization Potential (COP) index, introduced by White et al. (2018). COP assumes that larger and more closely spaced convective cores are more likely to interact, thereby contributing to organization. It yields a dimensionless value between 0 and 1, representing the degree of organization within a grid cell, by integrating the equivalent radii of cores and the pairwise distances between all cores. The second one, the Area-Based COP (ABCOP), is an adaptation of the original COP proposed by Jin et al. (2022). ABCOP enhances the COP framework by incorporating additional dependencies on the total area and the number of convective cores. The third diagnostic is the Radar Organization Metric (ROME), developed by Retsch et al. (2020). Unlike COP and ABCOP, ROME is expressed in surface units, with values ranging from one to two times the mean area of the convective cores. All three metrics share a common foundation in pairwise core analysis within a defined spatial domain.

Overall, these 3 metrics provide no clear separation between our two classes. The COP index exhibits an inverse trend, with highly structured scenes displaying lower COP values (Figure ~~15a~~16a, d). Among the three metrics, ROME provides the least effective class separation, particularly for the TOOCAN-radar dataset (Figure ~~15c~~16c, f). In contrast, the best separation is achieved using the ABCOP index (Figure ~~15b~~16b, e), especially in the TOOCAN-RCE dataset, although significant overlap remains in the central value range, particularly around 5 (unitless). ABCOP and ROME primarily reflect the total and mean convective object area, respectively (Mandorli et al. 2024), which corresponds to a combination of two of our four key ~~variables~~parameters (F and ~~S~~A). This partly explains the effective separation of the two most contrasted classes by these indices. However, the fact that ABCOP distinguishes the classes more effectively than ROME suggests that ~~while~~ organization is more strongly influenced by the total convective area (~~S), it~~A) than by the mean convective object area. Nevertheless, the overlaps within ABCOP distributions indicate that the complexity of spatial arrangements cannot be fully captured by ~~this single variable~~only A or even by its combination with F. This suggests that in order to achieve a more comprehensive distinction between different organizational patterns, spatial arrangement (L and P) has also to be considered.
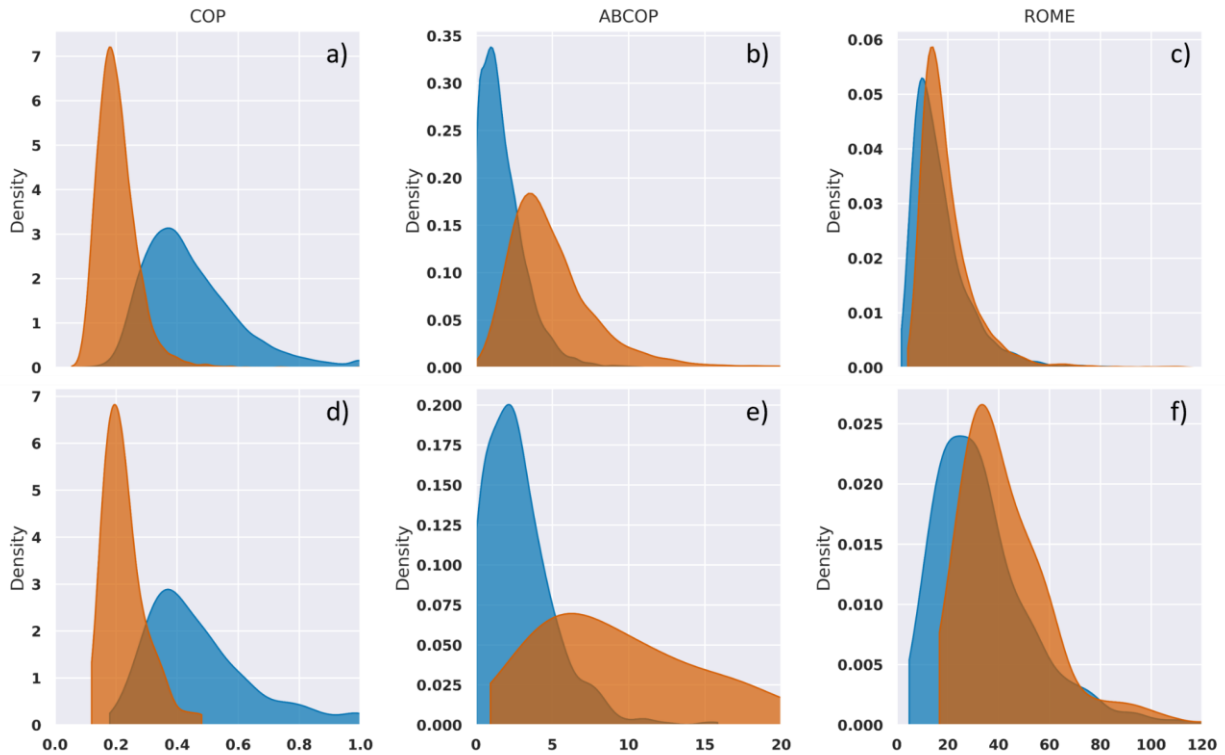
Figure ~~15~~16: Empirical probability density function (estimated via KDE) for the two extreme classes Top: 13443 scenes from TOOCAN-radar dataset, Bottom: 1055 scenes from TOOCAN-RCE dataset. a, d) COP index, b, e) ABCOP index, c, f) ROME index. Likely random (LR) are represented in blue while very structured (VS) scenes are colored in dark orange

Thus, attempting to define a single index to quantify convective organization seems very difficult, as convective structures exhibit complex spatial arrangements that cannot be fully captured by a single metric. A low dimensional characterization (e.g., the 4 key ~~variables~~parameters presented in this study) of convective organization is probably more appropriate as long as a comprehensive index that fully encapsulates this complexity has not yet been identified in the literature.

5 Conclusion

Organization of deep convection is crucial to better understand the role of deep convection in the climate system (Muller et al. 2022). In this study, a new method is introduced~~.~~ to quantify and characterize spatial arrangement of convective areas within a specific grid encompassing the instantaneous cloud shield of a deep convective system (DCS). This method extends previous works by i) considering a Lagrangian perspective, specifically by focusing on the spatial arrangement of deep convective cores within the cloud shield of the associated deep convective systems ~~(DCSs),~~, ii) extracting a characteristic scale of convective core distribution based on the spectral power of the scene computed via 2D autocorrelation, and iii) computing a statistic ensemble of convective scenes based on elementary decomposition and stochastic random generation, establishing a probabilistic distance from a random spatial organization. This distance, expressed as a ~~probability~~percentile (P), completes the characterization of each scene alongside its convection density (F), convective ~~surface (S~~area (A), and characteristic length (L). This subset of 4 ~~variables~~parameters describing deep convective organization aligns with the work of Janssens et al. 2021

714 suggesting that an effective low dimensional characterization of organization can be achieved. In this
715 work, the two more advanced ~~variables~~parameters L and P extend the analysis beyond F and ~~S~~A by
716 quantifying the spatial configuration of the cores and ~~the probability that the observed distribution~~
717 ~~deviates~~its deviation from randomness.

718 The robustness of the methodology is assessed by applying it to two independent datasets with distinct
719 convective core identification techniques, derived from satellite observations and kilometer-scale
720 numerical simulations. An unsupervised clustering approach is then employed to delineate four physically
721 sound organizational classes in both datasets. The resulting classification exhibits high consistency across
722 both datasets and quantifies the previously highlighted ambiguity found in existing organizational metrics
723 (Mandorli et al. 2024, Biagioli and Tompkins 2023).

724 The present approach has demonstrated good flexibility, effectively handling datasets with diverse scene
725 characteristics, including variations in size, convective fraction, and object count, while minimizing
726 arbitrary parameter choices and dataset dependencies, aligning with recent methodological
727 advancements (e.g., Koren et al., 2024). As convective organization spans a wide range of scales, from
728 isolated convective cores (≈5 km in diameter) to self-organized mesoscale convective systems with
729 diameters exceeding 100 km, exploring the scale independence and broader applicability of the present
730 method to such various fields or extending it to vertical velocities of updrafts in simulation or vertically
731 integrated precipitation from ground-based phased array radars would be one further promising
732 implication of this work. For instance, an adaptation to the spatial arrangement of DCS cloud shields within
733 a selected area, following Bony et al. (2020), could be considered using TOOCAN's segmentation as the
734 binary mask. However, this would require modifications, such as replacing (i) the elementary core
735 decomposition with convective system segmentation and (ii) the random generation process with
736 randomized positioning and orientation of them within the grid.

737 Examples of the potential applications of this method in weather and climate research include severe
738 weather and climate modelling. Establishing a statistical relationship between flooding (or strong wind
739 events) and the internal organization of convective systems would help nowcasting of these events by
740 completing the ingredients list (Doswell et al., 1996). Recent intercomparison exercises (Prein et al., 2024;
741 Feng et al., 2025) have revealed biases between the latest generation of km scale global models and the
742 satellite observed cloud shield morphology. The interpretation of these biases would benefit from
743 applying our method to these simulations to relate the limitations of the simulated morphology to that of
744 the convective organization as shown here.

745 One other venue for future work would be to extend the organization characterization with a time
746 dimension for datasets where this dimension is available such as ground-based radars and high-resolution
747 simulations. By incorporating time evolution of a selected field as a third dimension, the methodology
748 could assess spatiotemporal convective organization. Expanding the current 2D approach to a 3D
749 formulation will allow for a refined characterization of the temporality of convective organization,
750 reaching the individual dynamical convective cores life cycle scale in line with the work of Kim et al 2012
751 and Tseng et al. 2024)

752 In this study, specific methodological choices have been made regarding i) the elementary decomposition
753 into circular convective cores, ii) the stochastic generation model used to generate a distribution of
754 random scenes for quantifying deviations from randomness. One way to improve the first one would be
755 to work on the detection of the objects by implementing local maximum and water shading (or any other

756 region-growing techniques (Fiolleau et al. 2013) to a continuous field like precipitation for instance-). The
757 second point could be enhanced by exploring other generating processes with different random
758 probabilistic laws as the homogeneous Poisson point process (HPPP) (e.g., Savre 2024). In particular, these
759 refinements will help understand the underlying stochastic model governing organized convection and
760 will require dedicated work with a more systematic framework such as the one of Biagioli (2023).

761 Additionally, based on the TOOCAN-RCE dataset, or any dataset providing continuous fields across all time
762 steps, it becomes feasible to infer the temporal evolution of the four organizational ~~variables~~parameters:
763 $F(t)$, $S(t)$, $L(t)$, and $P(t)$. By tracking these metrics as functions of time, one can characterize the dynamical
764 evolution of the convective system's organization within the four-dimensional space. This time-resolved
765 approach enables a detailed assessment of how the degree and nature of organization evolve throughout
766 the lifecycle of the DCS, offering new insights into its developmental phases and potential transitions
767 between different organizational states.

768 Finally, the observational classified dataset is now being used to explore the relationship between
769 different organization patterns and the morphology of the associated convective systems. On-going
770 physically driven analysis shows promising results whereby the "organized" systems exhibit a scale
771 dependence sensitive to the depth of convection and will be further explored in upcoming studies.

772

Acknowledgments

774 We thank S. Cloché for her support with the handling of these various datasets. This study benefited from
775 the IPSL mesocenter ESPRI facility which is supported by CNRS, UPMC, Labex L-IPSL, CNES and Ecole
776 Polytechnique. The authors acknowledge the CNES and CNRS support under the Megha-Tropiques
777 program.

778

Open Research

780 The TOOCAN data are available from **http://toocan.ipsl.fr** with the with DOI
781 https://doi.org/10.14768/1be7fd53-8b81-416e-90d5-002b36b30cf8

782 The 2012-2020 homogenized infrared geostationary level-1C dataset described in this paper can be
783 accessed via the repository under the following data DOI: https://doi.org/10.14768/93f138f5-
784 a553-4691-96ed-952fd32d2fc3 (Fiolleau and Roca, 2023).

785 Toshio Iguchi, Robert Meneghini (2021), GPM DPR Precipitation Profile L2A 1.5 hours 5 km V07, Greenbelt,
786 MD, Goddard Earth Sciences Data and Information Services Center (GES DISC), Accessed:
787 10.5067/GPM/DPR/GPM/2A/07

788 The simulation data, along with the associated analyses, are currently in the process of being registered
789 and will be identified with a DOI to ensure persistent accessibility and citation.

6 References

Abramian, S., Muller, C., Risi, C., Fiolleau, T., Roca, R., 2025. How key features of early development shape deep convective systems. https://doi.org/10.21203/rs.3.rs-6614881/v1

Anber, U., Wang, S., Sobel, A., 2016. Response of Atmospheric Convection to Vertical Wind Shear: Cloud-System-Resolving Simulations with Parameterized Large-Scale Circulation. Part II: Effect of Interactive Radiation. https://doi.org/10.1175/JAS-D-15-0151.1

Awaka, J., Iguchi, T., Okamoto, K., 2009. TRMM PR Standard Algorithm 2A23 and its Performance on Bright Band Detection. Journal of the Meteorological Society of Japan. Ser. II 87A, 31–52. https://doi.org/10.2151/jmsj.87A.31

Awaka, J., Le, M., Brodzik, S., Kubota, T., Masaki, T., Chandrasekar, V., Iguchi, T., 2021. Development of Precipitation Type Classification Algorithms for a Full Scan Mode of GPM Dual-frequency Precipitation Radar. Journal of the Meteorological Society of Japan. Ser. II 99, 1253–1270. https://doi.org/10.2151/jmsj.2021-061

Awaka, J., Le, M., Chandrasekar, V., Yoshida, N., Higashiuwatoko, T., Kubota, T., Iguchi, T., 2016. Rain Type Classification Algorithm Module for GPM Dual-Frequency Precipitation Radar. https://doi.org/10.1175/JTECH-D-16-0016.1

Biagioli, G., 2023. Understanding deep convective organization: simple stochastic approaches and new metrics to bridge the gaps.

Biagioli, G., Tompkins, A.M., 2023. Measuring Convective Organization. Journal of the Atmospheric Sciences 80, 2769–2789. https://doi.org/10.1175/JAS-D-23-0103.1

Bony, S., Semie, A., Kramer, R.J., Soden, B., Tompkins, A.M., Emanuel, K.A., 2020. Observed Modulation of the Tropical Radiation Budget by Deep Convective Organization and Lower-Tropospheric Stability. AGU Advances 1, e2019AV000155. https://doi.org/10.1029/2019AV000155

Bryan, G.H., Wyngaard, J.C., Fritsch, J.M., 2003. Resolution Requirements for the Simulation of Deep Moist Convection.

Chen, Y., Wang, D., Zeng, Z., Huang, L., Li, E., Xue, Y., 2025. Observational structure and physical features of tropical precipitation systems. Atmospheric Research 315, 107885. https://doi.org/10.1016/j.atmosres.2024.107885

Doswell, C.A., Brooks, H.E., Maddox, R.A., 1996. Flash Flood Forecasting: An Ingredients-Based Methodology.

Elsaesser, G.S., Roca, R., Fiolleau, T., Del Genio, A.D., Wu, J., 2022. A Simple Model for Tropical Convective Cloud Shield Area Growth and Decay Rates Informed by Geostationary IR, GPM, and Aqua/AIRS Satellite Data. Journal of Geophysical Research: Atmospheres 127, e2021JD035599. https://doi.org/10.1029/2021JD035599

Feng, Z., Prein, A.F., Kukulies, J., Fiolleau, T., Jones, W.K., Maybee, B., Moon, Z.L., Núñez Ocasio, K.M., Dong, W., Molina, M.J., Albright, M.G., Rajagopal, M., Robledo, V., Song, J., Song, F., Leung, L.R., Varble, A.C., Klein, C., Roca, R., Feng, R., Mejia, J.F., 2025. Mesoscale Convective Systems Tracking Method Intercomparison (MCSMIP): Application to DYAMOND Global km-Scale Simulations. Journal of Geophysical Research: Atmospheres 130, e2024JD042204. https://doi.org/10.1029/2024JD042204

Fiolleau, T., Roca, R., 2024. A database of deep convective systems derived from the intercalibrated meteorological geostationary satellite fleet and the TOOCAN algorithm (2012–2020). Earth System Science Data 16, 4021–4050. https://doi.org/10.5194/essd-16-4021-2024

Fiolleau, T., Roca, R., 2013a. Composite life cycle of tropical mesoscale convective systems from geostationary and low Earth orbit satellite observations: method and sampling considerations. Quarterly Journal of the Royal Meteorological Society 139, 941–953. https://doi.org/10.1002/qj.2174

Fiolleau, T., Roca, R., 2013b. An Algorithm for the Detection and Tracking of Tropical Mesoscale Convective Systems Using Infrared Images From Geostationary Satellite. IEEE Transactions on Geoscience and Remote Sensing 51, 4302–4315. https://doi.org/10.1109/TGRS.2012.2227762

828 Fiolleau, T., Roca, R., Cloché, S., Bouniol, D., Raberanto, P., 2020. Homogenization of Geostationary Infrared Imager Channels for Cold
829   Cloud Studies Using Megha-Tropiques/ScaRaB. IEEE Transactions on Geoscience and Remote Sensing 58, 6609–6622.
830   https://doi.org/10.1109/TGRS.2020.2978171

831 Gallus, W.A., Snook, N.A., Johnson, E.V., 2008. Spring and Summer Severe Weather Reports over the Midwest as a Function of Convective
832   Mode: A Preliminary Study. https://doi.org/10.1175/2007WAF2006120.1

833 Haerter, J.O., Böing, S.J., Henneberg, O., Nissen, S.B., 2019. Circling in on Convective Organization. Geophysical Research Letters 46, 7024–
834   7034. https://doi.org/10.1029/2019GL082092

835 Holloway, C.E., Wing, A.A., Bony, S., Muller, C., Masunaga, H., L'Ecuyer, T.S., Turner, D.D., Zuidema, P., 2017. Observing Convective
836   Aggregation. Surv Geophys 38, 1199–1236. https://doi.org/10.1007/s10712-017-9419-1

837 Houze Jr., R.A., 2004. Mesoscale convective systems. Reviews of Geophysics 42. https://doi.org/10.1029/2004RG000150

838 Houze Jr., R.A., Betts, A.K., 1981. Convection in GATE. Reviews of Geophysics 19, 541–576. https://doi.org/10.1029/RG019i004p00541

839 Houze Jr., R.A., Rasmussen, K.L., Zuluaga, M.D., Brodzik, S.R., 2015. The variable nature of convection in the tropics and subtropics: A legacy
840   of 16 years of the Tropical Rainfall Measuring Mission satellite. Reviews of Geophysics 53, 994–1021.
841   https://doi.org/10.1002/2015RG000488

842 Houze Jr., R.A., Wilton, D.C., Smull, B.F., 2007. Monsoon convection in the Himalayan region as seen by the TRMM Precipitation Radar.
843   Quarterly Journal of the Royal Meteorological Society 133, 1389–1411. https://doi.org/10.1002/qj.106

844 Houze, R.A., 1997. Stratiform Precipitation in Regions of Convection: A Meteorological Paradox?

845 Janssens, M., Vilà-Guerau de Arellano, J., Scheffer, M., Antonissen, C., Siebesma, A.P., Glassmeier, F., 2021. Cloud Patterns in the Trades
846   Have Four Interpretable Dimensions. Geophysical Research Letters 48, e2020GL091001. https://doi.org/10.1029/2020GL091001

847 Ji, L., Xu, W., Chen, H., Liu, N., 2022. Consistency of Vertical Reflectivity Profiles and Echo-Top Heights between Spaceborne Radars Onboard
848   TRMM and GPM. Remote Sensing 14, 1987. https://doi.org/10.3390/rs14091987

849 Jin, D., Oreopoulos, L., Lee, D., Tan, J., Kim, K., 2022. A New Organization Metric for Synoptic Scale Tropical Convective Aggregation. Journal
850   of Geophysical Research: Atmospheres 127, e2022JD036665. https://doi.org/10.1029/2022JD036665

851 Khairoutdinov, M.F., Randall, D.A., 2003. Cloud Resolving Modeling of the ARM Summer 1997 IOP: Model Formulation, Results,
852   Uncertainties, and Sensitivities.

853 Kim, D.-S., Maki, M., Shimizu, S., Lee, D.-I., 2012. X-Band Dual-Polarization Radar Observations of Precipitation Core Development and
854   Structure in a Multi-Cellular Storm over Zoshigaya, Japan, on August 5, 2008. Journal of the Meteorological Society of Japan. Ser. II
855   90, 701–719. https://doi.org/10.2151/jmsj.2012-509

856 Knapp, K.R., Kruk, M.C., Levinson, D.H., Diamond, H.J., Neumann, C.J., 2010. The International Best Track Archive for Climate Stewardship
857   (IBTrACS). https://doi.org/10.1175/2009BAMS2755.1

858 Koren, I., Dror, T., Altaratz, O., Chekroun, M.D., 2024. Cloud Versus Void Chord Length Distributions (LvL) as a Measure for Cloud Field
859   Organization. Geophysical Research Letters 51, e2024GL108435. https://doi.org/10.1029/2024GL108435

860 Kukulies, J., Prein, A.F., Morrison, H., 2024. Simulating Precipitation Efficiency Across the Deep Convective Gray Zone. Journal of
861   Geophysical Research: Atmospheres 129, e2024JD041924. https://doi.org/10.1029/2024JD041924

862 Kummerow, C., Barnes, W., Kozu, T., Shiue, J., Simpson, J., 1998. The Tropical Rainfall Measuring Mission (TRMM) Sensor Package.

863 Lafore, J.P., Chapelon, N., Diop, M., Gueye, B., Largeron, Y., Lepape, S., Ndiaye, O., Parker, D.J., Poan, E., Roca, R., Roehrig, R., Taylor, C.,
864   Moncrieff, M., 2017. Deep Convection, in: Meteorology of Tropical West Africa. John Wiley & Sons, Ltd, pp. 90–129.
865   https://doi.org/10.1002/9781118391297.ch3

866   Lamer, K., Kollias, P., Luke, E.P., Treserras, B.P., Oue, M., Dolan, B., 2023. Multisensor Agile Adaptive Sampling (MAAS): A Methodology to
867   Collect Radar Observations of Convective Cell Life Cycle. https://doi.org/10.1175/JTECH-D-23-0043.1

868   Le, M., Chandrasekar, V., 2013. Precipitation Type Classification Method for Dual-Frequency Precipitation Radar (DPR) Onboard the GPM.
869   IEEE Transactions on Geoscience and Remote Sensing 51, 1784–1790. https://doi.org/10.1109/TGRS.2012.2205698

870   LeMone, M.A., Zipser, E.J., Trier, S.B., 1998. The Role of Environmental Shear and Thermodynamic Conditions in Determining the Structure
871   and Evolution of Mesoscale Convective Systems during TOGA COARE.

872   López, R.E., 1978. Internal Structure and Development Processes of C-Scale Aggregates of Cumulus Clouds.

873   Mandorli, G., Stubenrauch, C.J., 2024. Assessment of object-based indices to identify convective organization. Geoscientific Model
874   Development 17, 7795–7813. https://doi.org/10.5194/gmd-17-7795-2024

875   Mapes, B.E., 1993. Gregarious Tropical Convection.

876   Marinescu, P.J., van den Heever, S.C., Saleeby, S.M., Kreidenweis, S.M., 2016. The microphysical contributions to and evolution of latent
877   heating   profiles   in   two   MC3E   MCSs.   Journal   of   Geophysical   Research: Atmospheres   121,   7913–7935.
878   https://doi.org/10.1002/2016JD024762

879   Markowski,   P.,   Richardson,   Y.,   2010.   Mesoscale   Meteorology   in   Midlatitudes.   John   Wiley   and   Sons.
880   https://doi.org/10.1002/9780470682104

881   Moroda, Y., Tsuboki, K., Satoh, S., Nakagawa, K., Ushio, T., Shimizu, S., 2021. Structure and Evolution of Precipitation Cores in an Isolated
882   Convective Storm Observed by Phased Array Weather Radar. Journal of the Meteorological Society of Japan. Ser. II 99, 765–784.
883   https://doi.org/10.2151/jmsj.2021-038

884   Muller,   C.,   Bony,   S.,   2015.   What   favors   convective   aggregation   and   why?   Geophysical   Research   Letters   42,   5626–5634.
885   https://doi.org/10.1002/2015GL064260

886   Muller, C., Yang, D., Craig, G., Cronin, T., Fildier, B., Haerter, J.O., Hohenegger, C., Mapes, B., Randall, D., Shamekh, S., Sherwood, S.C.,
887   2022.   Spontaneous   Aggregation   of   Convective   Storms.   Annual   Review   of   Fluid   Mechanics   54,   133–157.
888   https://doi.org/10.1146/annurev-fluid-022421-011319

889   Prein, A.F., Feng, Z., Fiolleau, T., Moon, Z.L., Núñez Ocasio, K.M., Kukulies, J., Roca, R., Varble, A.C., Rehbein, A., Liu, C., Ikeda, K., Mu, Y.,
890   Rasmussen, R.M., 2024. Km-Scale Simulations of Mesoscale Convective Systems Over South America—A Feature Tracker
891   Intercomparison. Journal of Geophysical Research: Atmospheres 129, e2023JD040254. https://doi.org/10.1029/2023JD040254

892   Retsch, M.H., Jakob, C., Singh, M.S., 2020a. Assessing Convective Organization in Tropical Radar Observations. Journal of Geophysical
893   Research: Atmospheres 125, e2019JD031801. https://doi.org/10.1029/2019JD031801

894   Retsch, M.H., Jakob, C., Singh, M.S., 2020b. Assessing Convective Organization in Tropical Radar Observations. Journal of Geophysical
895   Research: Atmospheres 125, e2019JD031801. https://doi.org/10.1029/2019JD031801

896   Roca, R., Fiolleau, T., Bouniol, D., 2017. A Simple Model of the Life Cycle of Mesoscale Convective Systems Cloud Shield in the Tropics.
897   Journal of Climate 30, 4283–4298. https://doi.org/10.1175/JCLI-D-16-0556.1

898   Roca, R., Fiolleau, T., Elsaesser, G., 2024. Growth rate of deep convective system cloud shields: satellite observations and km-scale radiative
899   convective   equilibrium   simulations   (No.   EGU24-7675).   Presented   at   the   EGU24,   Copernicus   Meetings.
900   https://doi.org/10.5194/egusphere-egu24-7675

901   Romatschke, U., Houze, R.A., 2010. Extreme Summer Convection in South America. https://doi.org/10.1175/2010JCLI3465.1

902   Savre, J., 2024. Spatial Dispersion and Statistical Description of Organized Cumulus Cloud Ensembles in Radiative Convective Equilibrium.
903   Journal of Advances in Modeling Earth Systems 16, e2023MS004096. https://doi.org/10.1029/2023MS004096

904 Schiro, K.A., Sullivan, S.C., Kuo, Y.-H., Su, H., Gentine, P., Elsaesser, G.S., Jiang, J.H., Neelin, J.D., 2020. Environmental Controls on Tropical
905   Mesoscale Convective System Precipitation Intensity. Journal of the Atmospheric Sciences 77, 4233–4249.
906   https://doi.org/10.1175/JAS-D-20-0111.1

907 Semie, A.G., Bony, S., 2020. Relationship Between Precipitation Extremes and Convective Organization Inferred From Satellite
908   Observations. Geophysical Research Letters 47, e2019GL086927. https://doi.org/10.1029/2019GL086927

909 Skofronick-Jackson, G., Petersen, W.A., Berg, W., Kidd, C., Stocker, E.F., Kirschbaum, D.B., Kakar, R., Braun, S.A., Huffman, G.J., Iguchi, T.,
910   Kirstetter, P.E., Kummerow, C., Meneghini, R., Oki, R., Olson, W.S., Takayabu, Y.N., Furukawa, K., Wilheit, T., 2017. The Global
911   Precipitation Measurement (GPM) Mission for Science and Society. https://doi.org/10.1175/BAMS-D-15-00306.1

912 Stocker, E.F., Alquaied, F., Bilanow, S., Ji, Y., Jones, L., 2018. TRMM Version 8 Reprocessing Improvements and Incorporation into the GPM
913   Data Suite. https://doi.org/10.1175/JTECH-D-17-0166.1

914 Takahashi, H., Luo, Z.J., Stephens, G., Mulholland, J.P., 2023. Revisiting the Land-Ocean Contrasts in Deep Convective Cloud Intensity Using
915   Global Satellite Observations. Geophysical Research Letters 50, e2022GL102089. https://doi.org/10.1029/2022GL102089

916 Tobin, I., Bony, S., Roca, R., 2012. Observational Evidence for Relationships between the Degree of Aggregation of Deep Convection, Water
917   Vapor, Surface Fluxes, and Radiation. https://doi.org/10.1175/JCLI-D-11-00258.1

918 Tseng, C.-Y., Wang, L.-P., Onof, C., 2024. Modelling convective cell lifecycles with a copula-based approach. EGUsphere 1–33.
919   https://doi.org/10.5194/egusphere-2024-1540

920 Varble, A., Zipser, E.J., Fridlind, A.M., Zhu, P., Ackerman, A.S., Chaboureau, J.-P., Collis, S., Fan, J., Hill, A., Shipway, B., 2014. Evaluation of
921   cloud-resolving and limited area model intercomparison simulations using TWP-ICE observations: 1. Deep convective updraft
922   properties. Journal of Geophysical Research: Atmospheres 119, 13,891-13,918. https://doi.org/10.1002/2013JD021371

923 Weger, R.C., Lee, J., Zhu, T., Welch, R.M., 1992. Clustering, randomness and regularity in cloud fields: 1. Theoretical considerations. Journal
924   of Geophysical Research: Atmospheres 97, 20519–20536. https://doi.org/10.1029/92JD02038

925 White, B.A., Buchanan, A.M., Birch, C.E., Stier, P., Pearson, K.J., 2018. Quantifying the Effects of Horizontal Grid Length and Parameterized
926   Convection on the Degree of Convective Organization Using a Metric of the Potential for Convective Interaction. Journal of the
927   Atmospheric Sciences 75, 425–450. https://doi.org/10.1175/JAS-D-16-0307.1

928 Wing, A.A., Emanuel, K.A., 2014. Physical mechanisms controlling self-aggregation of convection in idealized numerical modeling
929   simulations. Journal of Advances in Modeling Earth Systems 6, 59–74. https://doi.org/10.1002/2013MS000269

930 Wing, A.A., Reed, K.A., Satoh, M., Stevens, B., Bony, S., Ohno, T., 2018. Radiative–convective equilibrium model intercomparison project.
931   Geoscientific Model Development 11, 793–813. https://doi.org/10.5194/gmd-11-793-2018

932 Wing, A.A., Stauffer, C.L., Becker, T., Reed, K.A., Ahn, M.-S., Arnold, N.P., Bony, S., Branson, M., Bryan, G.H., Chaboureau, J.-P., De Roode,
933   S.R., Gayatri, K., Hohenegger, C., Hu, I.-K., Jansson, F., Jones, T.R., Khairoutdinov, M., Kim, D., Martin, Z.K., Matsugishi, S., Medeiros,
934   B., Miura, H., Moon, Y., Müller, S.K., Ohno, T., Popp, M., Prabhakaran, T., Randall, D., Rios-Berrios, R., Rochetin, N., Roehrig, R.,
935   Romps, D.M., Ruppert Jr., J.H., Satoh, M., Silvers, L.G., Singh, M.S., Stevens, B., Tomassini, L., van Heerwaarden, C.C., Wang, S., Zhao,
936   M., 2020. Clouds and Convective Self-Aggregation in a Multimodel Ensemble of Radiative-Convective Equilibrium Simulations.
937   Journal of Advances in Modeling Earth Systems 12, e2020MS002138. https://doi.org/10.1029/2020MS002138

938 Zipser, E.J., Lutz, K.R., 1994. The Vertical Profile of Radar Reflectivity of Convective Cells: A Strong Indicator of Storm Intensity and Lightning
939   Probability?

940

Annex A: Decomposition into elementary cores:

Decomposition into elementary cores: methodology description

The decomposition process involves two main steps. The first is to find the maximum size of a square cluster that can fit within the mask: MaxSquareSize (Figure A1, middle). The algorithm scans the grid from top to bottom and left to right, assigning to each pixel the sum of its own value and the minimum value among the three neighboring pixels: the one above, the one to the left, and the one above-left. This step is illustrated in Figure A1, middle. The second step labels the structures based on the sizes identified in the first step, filling them from the largest clusters down to the 1x1 ones (Figure A1, right). As stated in the main text (see section 2.2), this partitioning algorithm could be non-unique, occurring in approximately 10% (TOOCAN-radar dataset) and 25% (TOOCAN-RCE dataset) of all scenes. This arises from the direction in which the partitioning algorithm scans the image pixels. However, a sensitivity analysis (not shown) revealed that this non-uniqueness has no significant effect on the subsequent methodology. There is no significant modification of the generated L distribution and therefore in the computation of the P value. Besides, the classification results remain consistent for over 99.6% of affected scenes in the TOOCAN-radar dataset and 95.6% in the TOOCAN-RCE dataset.
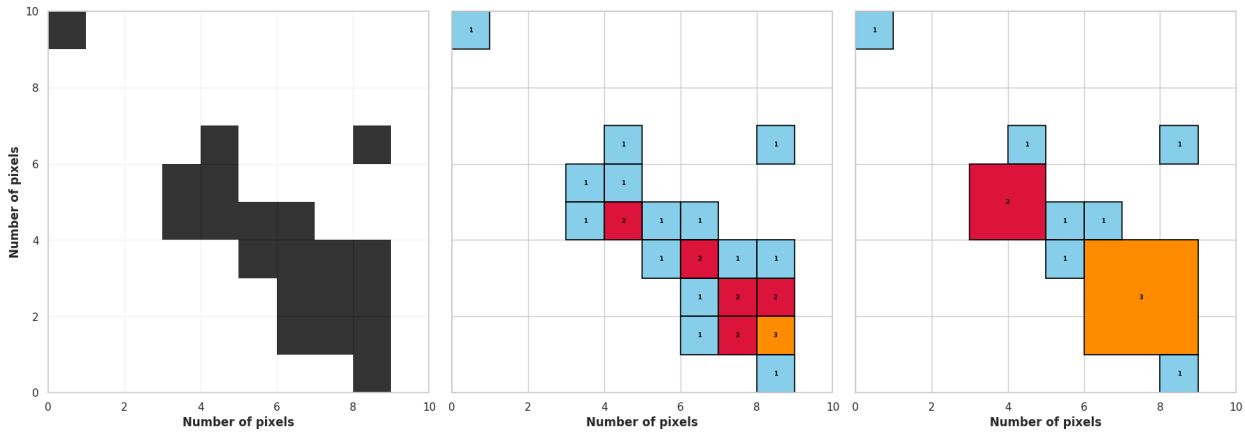
Figure A1: Left: 2D binary scene (convective mask). Middle: Identification of the maximum size (MaxSquareSize) within the grid before decomposition. Right: Elementary decomposition into square clusters.

Annex B: Sensitivity

Sensitivity to selected parameters

Threshold for computation of the autocorrelation characteristic scale

The 10% threshold T is modified to account for the sensitivity to this parameter. With T=5% and T=15%, the results for the L values differ slightly as the scale of the contour is directly impacted by this value. Figure ~~B2~~B1 shows the ~~realisations~~realizations of 500 generated L for various T thresholds. As T increases, the L values tend to decrease generally, but the P values do not vary much once compared to the generated L values obtained with the same T value. The major impact of T (and so its value definition) is on the L range but do not have major consequences in the classification process (e.g., Kmean used with normalized data)

For our usage in both convective areas from spaceborne radar and convective regions in simulations, the sensitivity study indicates that the 10% threshold remains the most suitable for encompassing a large diversity of scenes with a range of convective fractions between 0.5 to 25% without producing reasonable doubts in the classification process. It is noteworthy to be cautious for usage with convective fields that often count for more than 25% with large (up to 5 and more in size length) square elementary cores. We ~~prove (not shown)~~suggest that it ~~would~~could be interesting in such cases to increase the contour threshold up to 15~~%.~~% to better capture a proper range for L values.
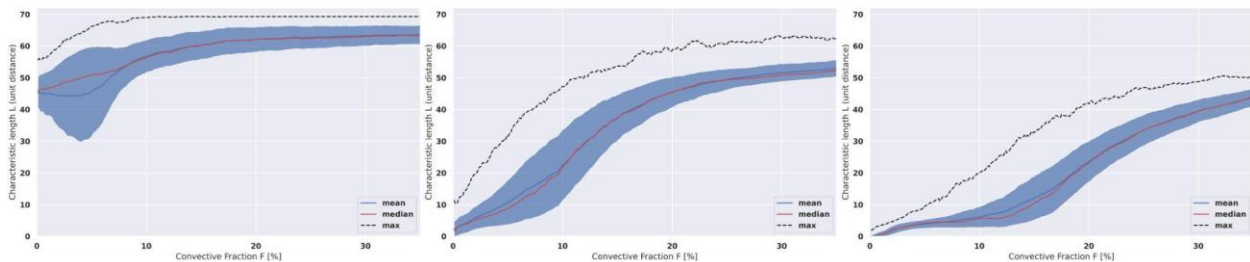
Figure B1: Same as figure ~~9~~10 with Left: T=5% threshold, Middle: T=10% threshold, Right: T=15% threshold for square clusters partition with MaxSquareSize <= 3.

~~Bootstrapping~~

Monte-Carlo approach for generating a random reference distribution

The same sensitivity study was conducted for the parameter regarding the amount of each ~~bootstrap~~Monte-Carlo generation of grids, with the number of generations being large enough to make a robust distribution. We came to the number of 500 as a perfectly suitable number of generated scenes for each real one, as a good compromise between computation time and statistical liability. With 500 iterations, the generated distributions of characteristic lengths exhibit a wide range of values with relatively smooth ~~histograms~~distributions, often exponential-like or with no common shape (Figure 9). The computation of P is always feasible, independently of the distribution shape.

992

993
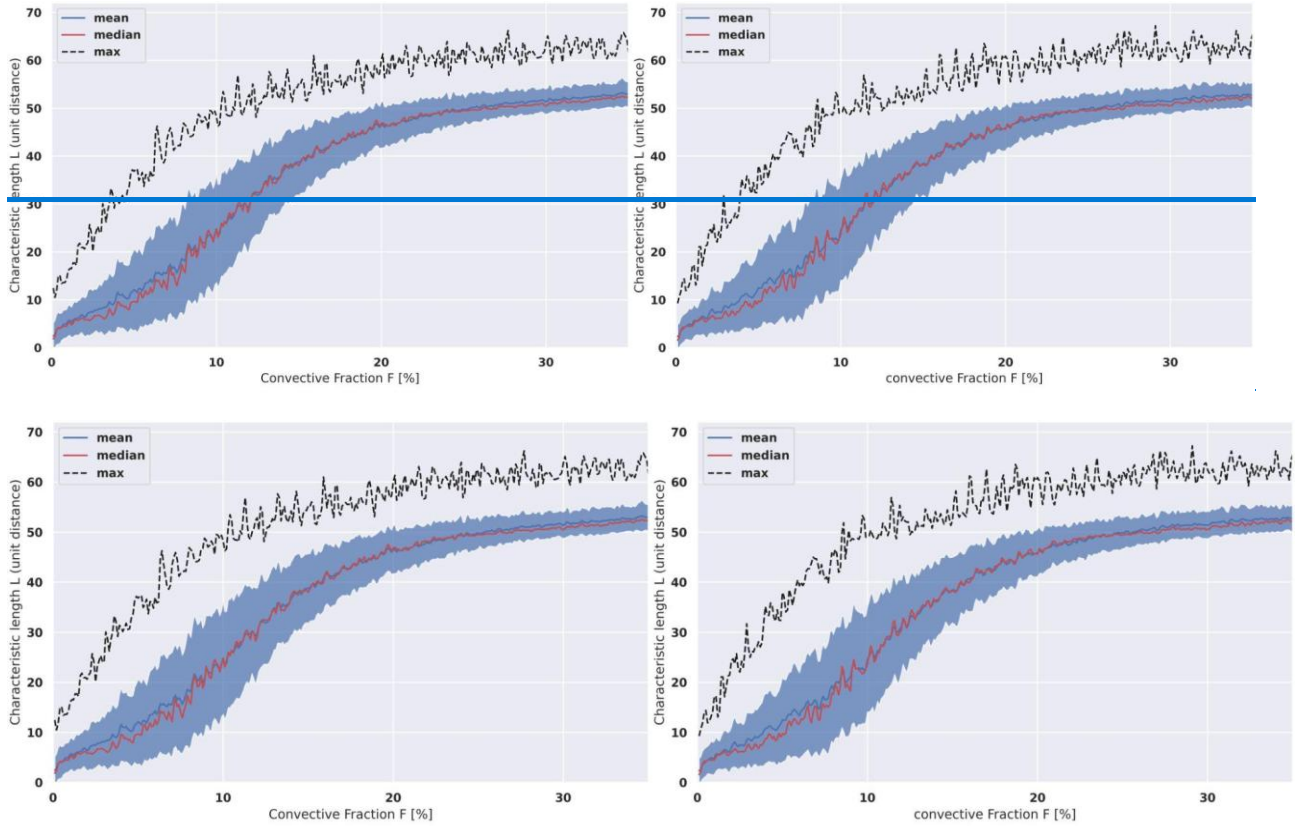
994   *Figure B2: Same as figure 910 with Left: 100 generations, Right: 1000 generations, for square clusters*
995   *partition with MaxSquareSize <= 3. Here there is a 0.5% rolling mean applied for readability and to allow*
996   *comparison.*

997

Monte-Carlo-style error estimation within the clustering algorithm

A Monte-Carlo-style study was conducted on K-means clustering, adding noise to each parameter in the radar dataset (~60,000 points). For each parameter, we added uniform noise with amplitude [-alpha/100*(Perc_90-Perc_10), +alpha/100*(Perc_90-Perc_10)], with alpha in % for values [0.5, 1, 2, 5, 10, 15, 20, 30]. Then we reclassify using the same Kmean algorithm (under the same conditions), and compare the class labels, calculating the number of points that change classes (or their proportion), the change in the silhouette score, and the Adjusted Rand Index (ARI), which quantifies the agreement between two partitions, correcting for random fluctuation. An ARI close to 1 means a very high correspondence between the two partitions, and when it approaches 0, we are close to an agreement corresponding to random draws. We perform this process 10 times for each value of alpha to estimate uncertainty on the mean values of each of the metrics, for each of the parameters. The results are presented in the figure below (that corresponds to the added Figure B3).

1010
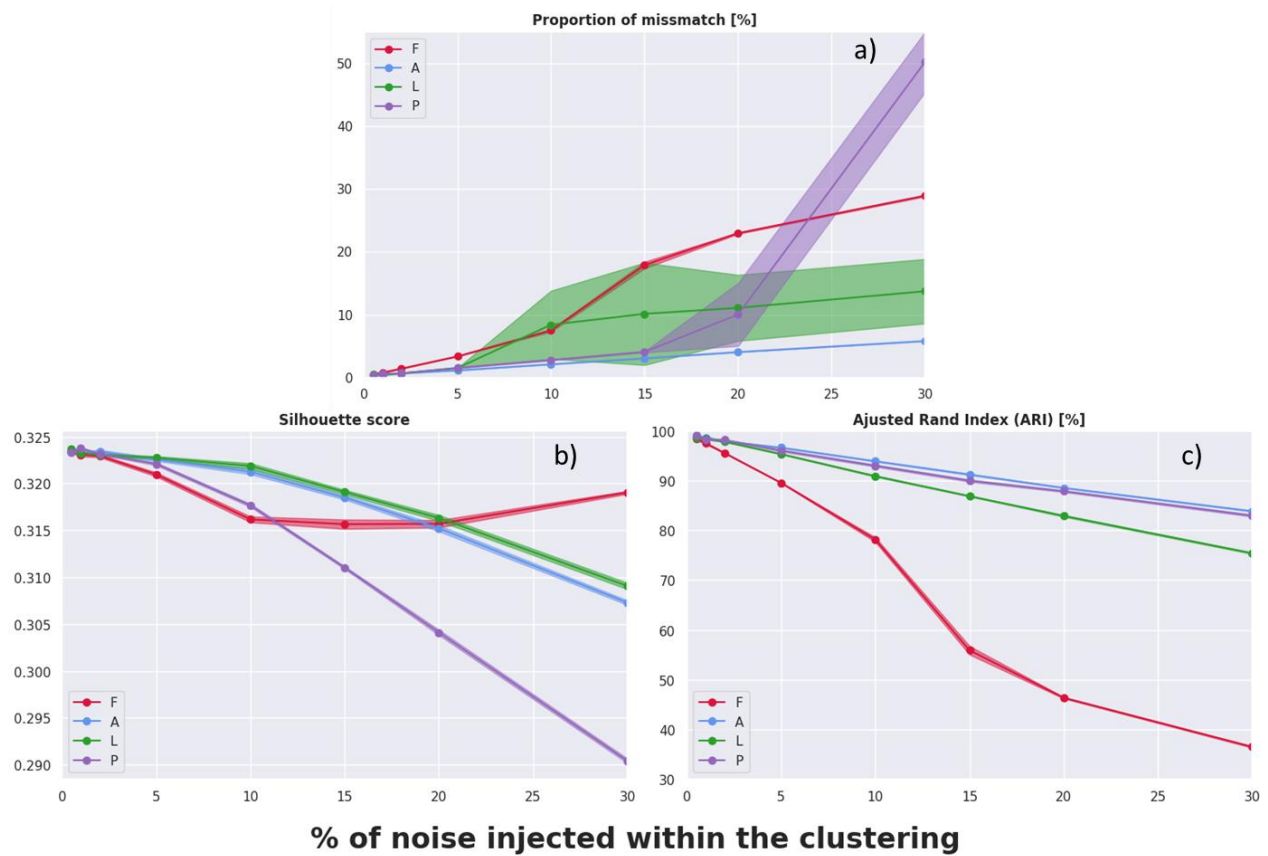
Figure B3: Variation in a) proportion of mismatch, b) Silhouette score, c) Adjusted Rand Index (ARI), comparing classification performance with perturbation by adding noise to the distributions of the four parameters (convective fraction (F), convective area (A), characteristic length (L) and percentile (P) shown in color), as a function of the percentage of noise added. The shaded areas correspond to the uncertainties for each measure (dots) computed as +/- 1 σ/√10 (10 being the number of carried experiments for each of the values).

This experiment allows to quantify systematic disturbance/error on each parameter and then define an order of importance regarding parameter sensitivity in the clustering process to perform classification. Based on the 3 metrics in Figure B3, A is the less impactful parameter when disturbed with noise, followed by P and L (depending on the index) when the percentage of noise is less than 15% which is already a significant change. Then F appears to be the dominant parameter, showing globally the highest (respectively lowest) scores in Figure B3a (resp. Figure B3b, c). Regarding the silhouette score, P becomes the dominating factor for alpha values higher than 15%, meaning that over this threshold for P, the centroids' position of the 4 classes become unstable. Overall, this demonstrates that up to +/- 5% noise on all parameters, the classification remains stable (with ARI>0.9, and even up to >10% for S, P, and L. Only F shows greater sensitivity above 10%. Moreover, the uncertainty estimated with 10 experiments for each of the selected set of parameters/alpha combination also shows that the method is statistically robust (shaded areas on Figure B3).